

## ON THE MEASUREMENT OF THE $^{13}\text{C}(\alpha, n)^{16}\text{O}$ $S$ -FACTOR AT NEGATIVE ENERGIES AND ITS INFLUENCE ON THE $s$ -PROCESS

M. LA COGNATA<sup>1</sup>, C. SPITALERI<sup>1,2</sup>, O. TRIPPELLA<sup>1,3</sup>, G. G. KISS<sup>1,4</sup>, G. V. ROGACHEV<sup>5</sup>, A. M. MUKHAMEDZHANOV<sup>6</sup>, M. AVILA<sup>5</sup>,  
G. L. GUARDO<sup>1,2</sup>, E. KOSHCHIY<sup>5</sup>, A. KUCHERA<sup>5</sup>, L. LAMIA<sup>2</sup>, S. M. R. PUGLIA<sup>1,2</sup>, S. ROMANO<sup>1,2</sup>, D. SANTIAGO<sup>5</sup>, AND R. SPARTÀ<sup>1,2</sup>

<sup>1</sup> Istituto Nazionale di Fisica Nucleare, Laboratori Nazionali del Sud, I-95123, Catania, Italy; lacognata@lns.infn.it

<sup>2</sup> Dipartimento di Fisica e Astronomia, Università di Catania, I-95123 Catania, Italy

<sup>3</sup> Istituto Nazionale di Fisica Nucleare, Sezione di Perugia, & Dipartimento di Fisica, Università di Perugia, I-06123 Perugia, Italy

<sup>4</sup> Institute of Nuclear Research (ATOMKI), Debrecen, Hungary

<sup>5</sup> Department of Physics, Florida State University, Tallahassee, FL, USA

<sup>6</sup> Cyclotron Institute, Texas A&M University, College Station, TX, USA

Received 2013 July 17; accepted 2013 September 16; published 2013 October 23

### ABSTRACT

The  $^{13}\text{C}(\alpha, n)^{16}\text{O}$  reaction is the neutron source for the main component of the  $s$ -process, responsible for the production of most of the nuclei in the mass range  $90 \lesssim A \lesssim 208$ . This reaction takes place inside the helium-burning shell of asymptotic giant branch stars, at temperatures  $\lesssim 10^8$  K, corresponding to an energy interval where the  $^{13}\text{C}(\alpha, n)^{16}\text{O}$  reaction is effective in the range of 140–230 keV. In this regime, the astrophysical  $S(E)$ -factor is dominated by the  $-3$  keV sub-threshold resonance due to the 6.356 MeV level in  $^{17}\text{O}$ , giving rise to a steep increase in the  $S$ -factor. Its contribution is still controversial as extrapolations, e.g., through the  $R$ -matrix and indirect techniques such as the asymptotic normalization coefficient (ANC), yield inconsistent results. The discrepancy amounts to a factor of three or more precisely at astrophysical energies. To provide a more accurate  $S$ -factor at these energies, we have applied the Trojan horse method (THM) to the  $^{13}\text{C}(^6\text{Li}, n)^{16}\text{O}$   $d$  quasi-free reaction. The ANC for the 6.356 MeV level has been deduced through the THM as well as the  $n$ -partial width, allowing us to attain unprecedented accuracy for the  $^{13}\text{C}(\alpha, n)^{16}\text{O}$  astrophysical factor. A larger ANC for the 6.356 MeV level is measured with respect to the ones in the literature,  $(\tilde{C}_{\alpha^{13}\text{C}}^{17\text{O}(1/2^+)})^2 = 7.7 \pm 0.3_{\text{stat}} \pm 1.6_{-1.5}^{\text{norm}} \text{ fm}^{-1}$ , yet in agreement with the preliminary result given in our preceding letter, indicating an increase of the  $^{13}\text{C}(\alpha, n)^{16}\text{O}$  reaction rate below about  $8 \times 10^7$  K if compared with the recommended values. At  $\sim 10^8$  K, our reaction rate agrees with most of the results in the literature and the accuracy is greatly enhanced thanks to this innovative approach.

*Key words:* nuclear reactions, nucleosynthesis, abundances – stars: AGB and post-AGB

*Online-only material:* color figures

### 1. INTRODUCTION

The origin of the chemical elements has been subject of quantitative studies since modern physics was born. Over the decades, its investigation has drawn the interest of cosmologists, astrophysicists, and astronomers, in addition to experimental, theoretical particle, and nuclear physicists.

Regarding heavy nuclides, in particular those having  $90 \lesssim A \lesssim 208$ , a major nucleosynthesis site has been identified as low-mass ( $\lesssim 3 M_{\odot}$ ), thermally pulsing asymptotic giant branch (AGB) stars (Meyer 1994), responsible for the production of heavy elements along the valley of stability through slow neutron captures (the  $s$ -process; Käppeler et al. 2011). In more detail, this is usually referred to as the main  $s$ -process component, as the understanding of isotopic abundances around  $A \sim 90$  has urged the introduction of the so-called weak component (The et al. 2000), which is believed to occur during the He-burning stage in the cores of massive stars ( $\geq 15 M_{\odot}$ ).

In AGB stars, hydrogen and helium are alternatively burned in shells surrounding a degenerate carbon-oxygen core. Helium burning occurs in pulses. Between pulses, hydrogen burns quiescently, building up a helium supply until a helium-burning flash is ignited. The liberated energy makes the star expand and quenches hydrogen burning. After the pulse has occurred, the star begins hydrogen-shell burning anew. Pulses last tens of years while interpulse periods last thousands of years. The complicated energy generation process characterizing AGB

stars and recursive mixing phenomena are able to expose nuclei to H burning and He burning as well. In addition, high neutron fluxes are found in the He-burning shell (Herwig 2005).

Each thermal pulse on the AGB provides favorable conditions for the convective dredge-up of material after the end of the flash-burning in the He shell (Herwig 2005). Dredge-up brings nucleosynthesis products from combined H- and He-shell burning to the surface; moreover, partial mixing at the interface between the convective and radiative regions admixes protons with  $^{12}\text{C}$ -rich material. Protons mixed downward are quickly captured by carbon nuclei, eventually leading to the formation of the so-called  $^{13}\text{C}$  pocket (Gallino et al. 1998). Then,  $^{13}\text{C}$  nuclei give up their excess neutrons to heavier nuclei through the  $^{13}\text{C}(\alpha, n)^{16}\text{O}$  reaction. This process is considered to be the main neutron supply providing the neutron flux necessary to build up heavy elements from iron-peak seed nuclei. Other processes, such as the  $^{22}\text{Ne}(\alpha, n)^{25}\text{Mg}$  reaction, can proceed efficiently only during He-shell flashes owing to the larger Coulomb barrier, yielding a limited amount of neutrons, not sufficient to sustain the  $s$ -process chain (Heil et al. 2008).

In the He-burning shell, temperatures vary between  $10^7$  and  $0.9 \times 10^8$  K during the time that the H-shell is the major nuclear source in the star, while temperatures can reach up to  $3 \times 10^8$  K during the He-burning phase (Straniero et al. 1995). At  $0.9 \times 10^8$  K, the energy range where the  $^{13}\text{C}(\alpha, n)^{16}\text{O}$  reaction is most effective, the so-called Gamow window (Iliadis 2007), is within  $\sim 140$ –230 keV. At such low energies region, direct cross

section measurements are exceedingly challenging because of the Coulomb barrier, exponentially suppressing the cross section, and the interplay between the rise of the astrophysical factor due to the sub threshold resonance at  $-3$  keV and the electron screening enhancement. For this reason, available direct experimental investigations (Davids 1968; Bair & Haas 1973; Kellogg et al. 1989; Brune et al. 1993; Drotleff et al. 1993; Harissopulos et al. 2005; Heil et al. 2008) could not cover the Gamow window. Therefore, a number of alternative experimental and theoretical approaches have been attempted in recent years to pin down the contribution of the sub threshold resonance.

## 2. STATE OF THE ART

### 2.1. Direct Measurements and Extrapolations

The most recent work on the  $^{13}\text{C}(\alpha, n)^{16}\text{O}$  reaction by Heil et al. (2008) combines a high-accuracy cross section measurement down to about 300 keV with an extensive  $R$ -matrix fitting of all cross section data for the channels leading to the population of  $^{17}\text{O}$  states (see Heil et al. 2008 and references therein).

The high-accuracy cross section data are used to renormalize previous  $^{13}\text{C}(\alpha, n)^{16}\text{O}$  datasets as they show a broad scatter in their absolute values (as large as a factor of two below about 1 MeV, as clearly shown in Figure 5 of Heil et al. 2008). Although there is good agreement between the  $S$ -factors of Davids (1968), Bair & Haas (1973), and Drotleff et al. (1993), Kellogg et al. (1989) reported a 30% smaller  $S(E)$ -factor. Such systematic discrepancies have been significantly reduced by the re-analysis by Brune et al. (1993), though these data are still inconsistent with the others as they are  $\sim 15\%$  smaller over the entire spanned energy range.

The need to reliably subtract a background in the observation of geo-neutrinos, e.g., in the KamLAND detector (Araki et al. 2005), triggered a new measurement of the  $^{13}\text{C}(\alpha, n)^{16}\text{O}$  reaction with the unprecedented accuracy of 4% (Harissopulos et al. 2005), cutting off at about 600 keV. Where available, this result supports the Kellogg et al. (1989) data, showing the same energy trend but a uniformly smaller absolute value, in comparison with the Davids (1968), Bair & Haas (1973), and Drotleff et al. (1993) preceding  $S(E)$ -factors. It is worth noting that the assessment of the  $^{13}\text{C}(\alpha, n)^{16}\text{O}$  cross section and astrophysical factor requires neutron detection, which might introduce systematic uncertainties due to, for instance, the evaluation of detection efficiency as a function of impinging neutron energies.

According to the discussion in Heil et al. (2008), the neutron efficiency in Harissopulos et al. (2005) was calculated by Monte Carlo simulations and checked against neutrons emitted by a  $^{252}\text{Cf}$  source. They are emitted with a Maxwellian spectrum with a mean energy of 2.3 MeV (Meadows 1967), while neutrons from the  $^{13}\text{C}(\alpha, n)^{16}\text{O}$  reaction are released with higher energies, owing to the 2.216 MeV reaction  $Q$ -value. Systematic errors in the detection efficiency could not be ruled out, possibly justifying the deviation of these data from those reported in Davids (1968), Bair & Haas (1973), Drotleff et al. (1993), and Heil et al. (2008). In this last work, by contrast, the neutron efficiency of the  $\text{BaF}_2$  calorimeter was measured using the  $^{51}\text{V}(p, n)^{51}\text{Cr}$  reaction in a setup identical to the one used to measure the  $^{13}\text{C}(\alpha, n)^{16}\text{O}$  reaction and simulated by means of the GEANT 4 toolkit. Accordingly, Heil et al. (2008) claim that the systematic uncertainty affecting their data is more accurately controlled and, consequently, the astrophysical factor

**Table 1**  
Summary of Astrophysical  $S$ -factors Evaluated  
at 100 keV by Different Authors

Reference	$S(100 \text{ keV})$ (MeVb)
Heil et al. (2008)	$3.3^{+1.8}_{-1.4} \times 10^6$
Descouvemont (1987)	$2.7 \times 10^6$
Dufour & Descouvemont (2005)	$5.3 \times 10^6$
Hale (1997)	$6.3 \times 10^6$
Johnson et al. (2006)	$1.2 \times 10^6$
Pellegriti et al. (2008)	$3.4 \times 10^6$
Guo et al. (2012)	$2.5^{+0.5}_{-0.6} \times 10^6$

of Harissopulos et al. (2005) was rescaled to match the one of Heil et al. (2008), as shown in Figure 18.

At the lowest energies, direct data, ending up at  $\sim 280$  keV (Drotleff et al. 1993), had to be corrected for atomic electron screening of the nuclear charges using the model of Rolfs & Rodney (1988). In the laboratory, projectiles and targets are in the form of ions and atoms or molecules, respectively, thus electron screening determines an exponential increase of  $S(E)$  for center-of-mass energies  $E_{\text{c.m.}} \rightarrow 0$  (Rolfs & Rodney 1988; Iliadis 2007), which is very different from electron screening in stars, where matter is in the form of plasma. Drotleff et al. (1993) considered an enhancement of less than 20% due to the electron screening of the nuclear charges for the lowest data point, corresponding to an electron screening potential of about 2.5 keV. Regardless, our current understanding of the electron screening effect is rather incomplete as experimental screening potentials exceed the theoretical upper limits in many cases (La Cognata et al. 2005; Aliotta et al. 2001; Engstler et al. 1992; Zahnnow et al. 1997; Angulo et al. 1993; Greife et al. 1995), although this is still debated (Barker 2002). Therefore, potential systematic errors might be introduced in the evaluation of the bare-nucleus astrophysical factor and, as a consequence, in its extrapolation to low energies.

Measurements aiming to cover the Gamow window are extremely challenging. Indeed, at  $\sim 300$  keV, corresponding to the minimum energy reached by direct investigations, the cross section of the  $^{13}\text{C}(\alpha, n)^{16}\text{O}$  reaction is already as low as  $\sim 10^{-10}$  b. For this reaction, the yield suppression is even more severe as the neutron detection efficiency is  $\sim 30\%$ , further reducing the signal-to-noise ratio.

The  $R$ -matrix approach (Lane & Thomas 1958) has been widely used to extrapolate the  $^{13}\text{C}(\alpha, n)^{16}\text{O}$  astrophysical factor down to  $\sim 100$  keV to cover the energy range of astrophysical relevance. In particular, Heil et al. (2008) employ a broad dataset including the renormalized  $^{13}\text{C}(\alpha, n)^{16}\text{O}$  astrophysical factors from Harissopulos et al. (2005), Kellogg et al. (1989), and Brune et al. (1993) to improve the determination of the tail of the  $-3$  keV sub-threshold resonance. By combining different datasets, generally with different systematic errors, a more accurate determination of the low-energy  $S$ -factor is expected. The extrapolated  $S$ -factor evaluated at 100 keV is given in Table 1. In any respect, as has been shown in Mukhamedzhanov et al. (2011), global fitting might turn out to be inaccurate precisely at astrophysical energies because of the unconstrained variations of some physical parameters. Moreover, our currently poor understanding of the electron screening effect might introduce systematic uncertainties in the extrapolation of the  $^{13}\text{C}(\alpha, n)^{16}\text{O}$  astrophysical factor down to  $\sim 100$  keV, owing to a flawed correction of the data points close to the Gamow window.

**Table 2**  
Summary of ANC Values  $(\tilde{C}_{\alpha^{13}\text{C}}^{17\text{O}(1/2^+)})^2$  and the Spectroscopic Factors  $S_\alpha$  in the Literature

Reference	$(\tilde{C}_{\alpha^{13}\text{C}}^{17\text{O}(1/2^+)})^2$ (fm <sup>-1</sup> )	$S_\alpha$
Johnson et al. (2006)	$0.89 \pm 0.23$	...
Kubono et al. (2003)	...	0.011
Keeley et al. (2003)	...	0.36–0.40
Pellegriti et al. (2008)	$4.5 \pm 2.2$	$0.29 \pm 0.11$
Guo et al. (2012)	$4.0 \pm 1.1$	$0.37 \pm 0.12$

Independent theoretical calculations have also been proposed to advance the description of the low-energy cross section, where experimental information is still missing. Descouvemont (1987) and Dufour & Descouvemont (2005) used a microscopic cluster approach defining bound, resonant, and scattering wave functions in the generator coordinate method. In microscopic models, as soon as the nucleon–nucleon interaction is chosen, no degrees of freedom are left and some partial widths could not be appropriately reproduced (Dufour & Descouvemont 2005). The calculated astrophysical factor at 100 keV is shown for comparison in Table 1. Taking into account the large uncertainties in the data and the calculations, the agreement is fair.

It is worth mentioning that in the NACRE compilation (Angulo et al. 1999), the  $S$ -factor was extrapolated by fitting the data of Drotleff et al. (1993), including the tail of the sub-threshold resonance at  $-3$  keV. The result was in agreement with the earlier  $R$ -matrix calculation by Hale (1997; check Table 1). This calculation yielded a significantly larger  $S$ -factor than those reported in Heil et al. (2008).

Discrepancies with other  $R$ -matrix calculations (Hale 1997) and with advanced theoretical calculations, such as the microscopic two-cluster model (Descouvemont 1987; Dufour & Descouvemont 2005), might point to incomplete knowledge of the low energy  $^{13}\text{C}(\alpha, n)^{16}\text{O}$   $S(E)$ -factor. This has called for independent measurements using, for instance, indirect methods.

## 2.2. Indirect Measurements

Indirect techniques make use of well-established nuclear reaction models, such as the Distorted Wave Born Approximation (DWBA), the Continuum Discretized Coupled Channel, or the Glauber approximation, to perform a easier quantitative evaluation of the cross section of a reaction of astrophysical relevance starting from a different reaction. Alternative approaches using indirect methods have then been undertaken to determine the resonance parameters of the 6.356 MeV  $^{17}\text{O}$  state. In particular, the determination of the asymptotic normalization coefficient (ANC; Mukhamedzhanov et al. 1997) through  $\alpha$ -transfer reactions represents a very useful tool. Indeed, the Coulomb-modified ANC  $\tilde{C}_{\alpha^{13}\text{C}}^{17\text{O}(1/2^+)}$  of the  $-3$  keV resonance is the principal parameter needed to calculate the  $^{13}\text{C}(\alpha, n)^{16}\text{O}$  astrophysical factor at low energies, where the  $S$ -factor is dominated by the 6.356 MeV  $^{17}\text{O}$  state, assuming the value given in the literature (Tilley et al. 1993) for the neutron partial width.

Johnson et al. (2006) extracted the 6.356 MeV state ANC from the  $^6\text{Li}(^{13}\text{C}, d)^{17}\text{O}$  sub-Coulomb  $\alpha$ -transfer reaction, obtaining  $(\tilde{C}_{\alpha^{13}\text{C}}^{17\text{O}(1/2^+)})^2 = 0.89 \pm 0.23$  fm<sup>-1</sup> (Table 2). In comparison with the determination of the  $S_\alpha$  spectroscopic factor of the 6.356 keV state of  $^{17}\text{O}$ , better accuracy can be achieved using the ANC since it is almost independent of the optical model potential parameters used to fit the transfer reaction cross

sections; the sub-Coulomb transfer reaction is a peripheral process. It turns out that the contribution to the overall uncertainty affecting the ANC of the 6.356 MeV level, imputable to theoretical analysis, is less than 20% if the parameters are kept within reasonable limits. The  $(\tilde{C}_{\alpha^{13}\text{C}}^{17\text{O}(1/2^+)})^2$  was introduced into a two-channel  $R$ -matrix calculation to obtain the total  $S$  factor of the  $^{13}\text{C}(\alpha, n)^{16}\text{O}$  process. In order to achieve a satisfactory fit to the available direct data, a constant non-resonance contribution of  $(0.4 \pm 0.2) \times 10^6$  MeVb was added to the astrophysical factor. The low-energy  $S$ -factor, including the contribution of the  $-3$  keV resonance calculated by means of the measured ANC, turned out to be much smaller than the one given in Heil et al. (2008) and in Angulo et al. (1999), commonly adopted in  $s$ -process modeling. This is clearly shown in Table 1, where the  $S$ -factor calculated at 100 keV is displayed; Johnson et al. (2006) report a value of  $1.2 \times 10^6$  MeVb, about three times smaller than the Heil et al. (2008) result and five times smaller than the NACRE one (Angulo et al. 1999). Consequently, at temperatures significant for the  $s$ -process in AGB stars, the reaction rate calculated by Johnson et al. (2006) is smaller by a factor of three than that adopted in the NACRE compilation.

The  $S_\alpha$  spectroscopic factor has been determined by several authors by means of transfer reactions such as  $^{13}\text{C}(^6\text{Li}, d)^{17}\text{O}$  (Kubono et al. 2003; Keeley et al. 2003) and  $^{13}\text{C}(^7\text{Li}, t)^{17}\text{O}$  (Pellegriti et al. 2008), when performing a DWBA analysis. As discussed in Kubono et al. (2003), for instance, the  $\alpha$ -width of a resonance is proportional to the  $S_\alpha$  spectroscopic factor; thus, its determination unequivocally determines the contribution of the 6.356 MeV state to the astrophysical factor, using the neutron partial width available in the literature (Tilley et al. 1993).

Kubono et al. (2003) suggested a very small  $\alpha$ -width for the 6.356 MeV state from their deduced  $S_\alpha = 0.011$  (Table 2), in contradiction with the spectroscopic factors usually adopted in  $s$ -process models ( $S_\alpha = 0.3$ – $0.7$ ) and the more recent results in Heil et al. (2008) and Johnson et al. (2006). Kubono et al. (2003) quantified a  $\sim 5\%$  uncertainty on  $S_\alpha$  due to different combinations of the optical potential sets. It is worth mentioning that Kubono et al. (2003) re-normalized their deduced spectroscopic factor to account for the difficulty of the exact treatment of the cluster structure in the DWBA formalism, taking as a reference the 3.055 MeV state, which is known to be a good  $\alpha$ -cluster state ( $S_\alpha = 0.25$ ). Even assuming  $S_\alpha = 1$  for this state, a maximum  $S_\alpha = 0.044$  would be obtained for the 6.356 MeV level, ruling out a possible  $\alpha$ -cluster structure for this  $^{17}\text{O}$  state.

Keeley et al. (2003) re-analyzed the Kubono et al. (2003) data using both the DWBA and a coupled reaction channels analysis. In more detail, adopting the same optical potential parameters as those used by Kubono et al. (2003), Keeley et al. (2003) obtained  $S_\alpha = 0.49$ , well within the range used in astrophysical calculations. Changing the optical potential parameters and after the renormalization procedure described in Kubono et al. (2003),  $S_\alpha = 0.15$  was deduced, one order of magnitude larger than what was reported in the original work. Thanks to an improved DWBA analysis, Keeley et al. (2003) suggested  $S_\alpha = 0.36$ , in agreement with the result from the coupled reaction channels analysis ( $S_\alpha = 0.40$ ; Keeley et al. 2003) and with the stronger contribution suggested in more recent works by Heil et al. (2008) and Johnson et al. (2006).

Pellegriti et al. (2008) measured  $S_\alpha = 0.29 \pm 0.11$  using the  $^{13}\text{C}(^7\text{Li}, t)^{17}\text{O}$  reaction at two incident energies, 28 and 34 MeV. The use of  $^7\text{Li}$  in the place of  $^6\text{Li}$  reduced possible multistep effects and enhanced the transfer cross sections to

low-spin states, although this required the evaluation of the spectroscopic factor for the overlap between  $\alpha + t$  and  ${}^7\text{Li}$ . Having two runs at different beam energies afforded an opportunity to check the direct mechanism characteristics of the transfer process. Using the optical potential parameters describing their experimental angular distributions, the Coulomb-modified ANC  $(\tilde{C}_{\alpha^{13}\text{C}}^{17\text{O}(1/2^+)})^2 = 4.5 \pm 2.2 \text{ fm}^{-1}$  was calculated;  $S_\alpha$  and  $(\tilde{C}_{\alpha^{13}\text{C}}^{17\text{O}(1/2^+)})^2$  are reported in Table 2. Pellegriti et al. (2008) performed a very careful test of the sensitivity of the spectroscopic factor to the DWBA parameters. They found a maximum spreading of 20% on the cross section when varying the entrance and exit optical potential parameters, the same spreading when varying the well geometry parameters, and a  $\sim 28\%$  deviation when the incident energy changes from 28 to 34 MeV. Notwithstanding the large uncertainties deriving from the DWBA analysis, the Coulomb-modified ANC in Pellegriti et al. (2008) is five times larger than the one determined in Johnson et al. (2006). From the experimental  $S_\alpha$ , the reduced width  $\gamma_\alpha$  of the 6.356 MeV level was also calculated and introduced in a  $R$ -matrix fit of the existing  ${}^{13}\text{C}(\alpha, n){}^{16}\text{O}$  data to extrapolate the  $S$ -factor down to astrophysical energies. The obtained result is in agreement with the one in Heil et al. (2008), which was used to calculate the reaction rate at temperatures between  $8\text{--}10 \times 10^7$  K, important for the  $s$ -process in low mass AGB stars. These authors inferred a value at  $0.9 \times 10^8$  K that was 2.3 times larger than the one in Johnson et al. (2006) and 1.3 smaller than the one in the NACRE compilation (Angulo et al. 1999).

Recently, Guo et al. (2012) reported a new measurement of the  $\alpha$ -spectroscopic factor and the ANC of the 6.356 MeV  $1/2^+$  sub-threshold state of  ${}^{17}\text{O}$  through the  ${}^{13}\text{C}({}^{11}\text{B}, {}^7\text{Li}){}^{17}\text{O}$  transfer reaction. They used a  ${}^{13}\text{C}$ -enriched target (with an initial  ${}^{13}\text{C}$  content of 88%); due to the presence of  ${}^{12}\text{C}$  in the  ${}^{13}\text{C}$  target, the  ${}^7\text{Li}$  events from the  ${}^{13}\text{C}({}^{11}\text{B}, {}^7\text{Li}){}^{17}\text{O}^*$  (6.356 MeV) reaction were mixed with those from the  ${}^{12}\text{C}({}^{11}\text{B}, {}^7\text{Li}){}^{16}\text{O}^*$  (6.917 MeV) reaction. To evaluate this background, the  $({}^{11}\text{B}, {}^7\text{Li})$  reactions were measured for both the  ${}^{13}\text{C}$  target and a  ${}^{12}\text{C}$  target at each angle with the same experimental setup. It turned out that the background from  ${}^{12}\text{C}$  accounted for approximately half of the total events from the  ${}^{13}\text{C}$  target. The resulting angular distributions were fit to deduce the  $S_\alpha$  parameter. For this purpose, Guo et al. (2012) first calculated the spectroscopic amplitudes of the  $\alpha$ -cluster in the ground state of  ${}^{11}\text{B}$ ; then, 81 sets of geometry parameters were obtained and used to calculate 81 values of  $S_\alpha$  and  $(\tilde{C}_{\alpha^{13}\text{C}}^{17\text{O}(1/2^+)})^2$ . Their standard deviations were taken as the uncertainty derived from the geometry parameters of  ${}^{17}\text{O}$ ; the best-fit values are displayed in Table 2 and are in good agreement with Keeley et al. (2003) and Pellegriti et al. (2008), with reduced uncertainty. This is due to the great care taken in the investigation of the sensitivity of the spectroscopic factor and the ANC on the geometry parameters and the possible neglect of the increase of  $S_\alpha$  for the increasing beam energy already observed by Pellegriti et al. (2008), which significantly contributes to the overall uncertainty. Finally, Guo et al. (2012) calculated the  $S$ -factor using the Breit-Wigner formula, evaluating the  $\alpha$ -width of the  $-3$  keV resonance from the deduced spectroscopic factor. The  $S$ -factor at 100 keV shown in Table 1 is in good agreement, within the uncertainties, with the value given in Pellegriti et al. (2008) and Heil et al. (2008). The reaction rate at  $0.9 \times 10^8$  K is about 10% smaller than the one determined by Heil et al. (2008), but the uncertainty has been reduced from  $\sim 22\%$  to  $\sim 17\%$ .

From the discussion so far and the numbers reported in Tables 1 and 2, it is apparent that the extrapolated  $S$ -factors,

as well as the 6.356 MeV  ${}^{17}\text{O}$  level parameters, are subject to significant scatter due to the presence of systematic errors. Ambiguities in the reaction mechanism (direct transfer or compound nucleus), finite energy resolution, detection thresholds, and background due to, for instance,  ${}^{12}\text{C}$  impurities in the enriched  ${}^{13}\text{C}$  target, might be responsible for such inconsistencies between the indirect measurements and the extrapolations, calling for further work before drawing definite conclusions on the contribution of the crucial  $-3$  keV sub-threshold resonance in the  ${}^{13}\text{C}(\alpha, n){}^{16}\text{O}$  reaction.

### 3. THE THM FRAMEWORK

The Trojan horse method (THM) might provide an important contribution to the understanding of the low-energy behavior of the  ${}^{13}\text{C}(\alpha, n){}^{16}\text{O}$   $S$ -factor as it allows one to study a reactions of astrophysical interest free of Coulomb suppression and electron screening at astrophysical energies with no need for extrapolation (see Spitaleri et al. 2011 for a review of the method). The Coulomb barrier decreases the cross section down to picobarn values and smaller, making it impossible to extend the cross sectional measurement down to astrophysical energies. Even if such measurements were possible (for instance, in underground laboratories; Fiorentini et al. 1995), electron screening would hide the nuclear cross section, which is the parameter of interest for astrophysical applications.

In the laboratory, electron screening enhances the cross section, compared with the value it would assume if nuclei were fully stripped of their electrons, when the classical distance of closest approach draws close to the atomic radius. In fact, electron clouds partially shield nuclear charges, reducing the Coulomb suppression effect. In stellar plasmas, nuclei are fully stripped of their electrons because of the high temperatures in the inner stellar layers and screening is induced by free electrons, gathering around positively charged nuclei in the so-called Debye sphere. Therefore, electron screening acts differently in the laboratory and in stellar plasma (Rolfs & Rodney 1988), making extrapolation necessary in any case. At present, our understanding of electron screening is inadequate, as discussed above. Correcting for electron screening enhancement to extract the bare-nucleus astrophysical  $S(E)$ -factor might introduce systematic errors. Moreover, if the corrected data are extrapolated to astrophysical energies, the reaction rate at the temperatures of interest might be inaccurate.

In the THM approach, the low-energy cross section of an  $A(x, c)C$  reaction is obtained by extracting the quasi-free (QF) contribution to a suitable  $A(a, c)C$  reaction. In QF kinematics, particle  $a$ , characterized by a prominent  $x \oplus s$  cluster structure, is used to transfer the participant cluster  $x$  and feed the excited states of the  $F = c + C$  system, while the other constituent cluster  $s$  is emitted without interacting with the system  $F$ , thus behaving as a spectator to the  $A(x, c)C$  sub-process. The QF reaction mechanism is sketched in Figure 1. Particle  $x$  is virtual, namely, the mass-shell equation is not satisfied for it. Therefore, the  $A(x, c)C$  sub reaction is half-off-energy-shell (HOES) as fragments  $c$  and  $C$  in the exit channel are real. Cross sections obtained using direct approaches are on-energy-shell (OES) as particles in the entrance and exit channels are all real, thus the HOES cross section cannot be right juxtaposed to the direct one. Since part of the projectile energy is spent to break the Trojan horse (TH) nucleus  $a$  and thanks to the  $x$ - $s$  inter cluster motion, astrophysical energies can be achieved in the  $A - x$  entrance channel of the TH reaction using beam energies of few

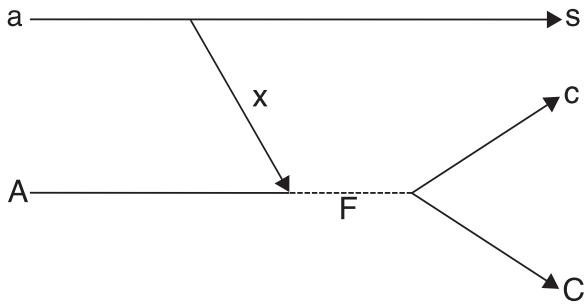


**Figure 1.** Sketch of the QF reaction mechanism, in the case of a resonance sub reaction  $A + x \rightarrow c + C$ . Nucleus  $a$  breaks up into fragments  $x$  and  $s$  in the nuclear field of  $A$ . While  $x$  is captured by  $A$ , leading to the formation of the compound system  $F$ ,  $s$  flies away without influencing either the  $A + x \rightarrow F$  fusion or the subsequent  $F \rightarrow c + C$  decay.

tens of MeV, bypassing the Coulomb barrier and the electron screening enhancement.

The THM has proved successful in the investigation of several resonant and non-resonant reactions of astrophysical and fundamental nuclear physics importance, such as the  $p + p$  elastic scattering (Tumino et al. 2007, 2008), the  $^{19}\text{F}(p, \alpha)^{16}\text{O}$  (La Cognata et al. 2011), the  $^{17}\text{O}(p, \alpha)^{14}\text{N}$  (Sergi et al. 2010), the  $^9\text{Be}(p, \alpha)^6\text{Li}$  (Romano et al. 2006), and the  $^6\text{Li}(n, \alpha)^3\text{H}$  reactions (Gulino et al. 2010). In a recent letter (La Cognata et al. 2012), the THM was first used to deduce the resonance parameters of a sub-threshold level, the 6.356 MeV state in  $^{17}\text{O}$  leading to a resonance at  $-3$  keV in the  $^{13}\text{C}(\alpha, n)^{16}\text{O}$   $S$ -factor. In this way, the low-energy trend of the astrophysical factor was indirectly established.

The reason why negative energies in the  $A - x$  channel can be investigated can be understood if energy and momentum conservation in the three-ray vertex,  $a \rightarrow s + x$ , and in the four-ray vertex,  $A + x \rightarrow C + c$ , of the pole diagram of Figure 1 are examined. Using  $\varepsilon_{ij}$ ,  $E_{ij}$ , and  $p_{ij}$  to refer to the binding energy, the relative energy, and the relative momentum of particles  $i$  and  $j$ , respectively, La Cognata et al. (2007) concluded that:

$$E_{Ax} = \frac{p_{Ax}^2}{2\mu_{Ax}} - \frac{p_{sx}^2}{2\mu_{sx}} - \varepsilon_{sx}, \quad (1)$$

where  $\mu_{ij}$  is the reduced mass of the  $i-j$  system. Assuming that the  $x-s$  relative motion takes place in  $s$ -waves (like the  $p-n$  motion inside deuterons or the  $d-\alpha$  motion inside  $^6\text{Li}$ ), in QF kinematics,  $p_{sx} = 0$  and

$$E_{Ax} = \frac{p_{Ax}^2}{2\mu_{Ax}} - \varepsilon_{sx}. \quad (2)$$

By choosing a suitable beam energy and TH nucleus, negative energies can be attained in QF kinematics, even if the energy of projectile  $A$  exceeds the Coulomb barrier in the initial channel,  $A + a$ , of the TH reaction, owing to the binding energy  $\varepsilon_{sx}$ . Moreover, Equation (2) shows that the mass shell equation is not satisfied for the  $A - x$  system, namely  $E_{Ax} \neq p_{Ax}^2/2\mu_{Ax}$ , because the transferred particle  $x$  is virtual. La Cognata et al. (2007) also noted that the energy  $E_{Ax}$  is uniquely determined by the incident beam energy  $E_A$  in QF kinematics. Hence, determining the energy dependence of the binary reaction cross section from the TH reaction would require continuously changing the beam energy. The entire Gamow window (Rolfs & Rodney 1988; Iliadis 2007) can be covered with a single beam energy  $E_A$  if small deviations from the QF conditions are

considered, that is, by varying the relative momentum  $p_{sx}$  in the interval  $0 \leq p_{sx} \leq p_{sx}^{(\max)} < \kappa_{sx}$ , where  $\kappa_{sx} = \sqrt{2\mu_{sx}\varepsilon_{sx}}$  is the  $a = s \oplus x$  bound-state wave number (La Cognata et al. 2007; Shapiro 1967). Under the simplifying hypothesis that the TH nucleus is at rest in the laboratory system, Equation (1) takes the form:

$$E_{Ax} = \frac{m_x}{m_x + m_A} E_A - \frac{p_s^2}{2\mu_{sF}} + \frac{\mathbf{p}_s \cdot \mathbf{p}_A}{m_x + m_A} - \varepsilon_{sx}, \quad (3)$$

where  $m_i$  and  $p_i$  are the mass and momentum of the  $i$ th particle. Therefore, the energy range relevant for astrophysics can be covered at a fixed beam energy by varying the absolute value and/or the direction of the spectator momentum in the laboratory system. The accessible energy range is fixed by the cutoff  $p_{sx}^{(\max)}$  in the momentum distribution of the Fermi motion for  $s$  and  $x$  inside  $a$ . Similar results are obtained in the case of projectile breakup, when the TH nucleus is not at rest, by means of a change of reference frame.

In general, the TH reaction amplitude describing the transfer of a particle  $x$  is given in the post form by (for simplicity, we disregard particle spins)

$$M(P, \mathbf{k}_{aA}) = \langle \chi_{\mathbf{k}_{sF}}^{(-)} \Phi_F^{(-)} | \Delta V_{sF} | \Psi_i^{(+)} \rangle. \quad (4)$$

Here,  $\Psi_i^{(+)}$  is the exact  $a + A$  scattering wave function,  $\Phi_F^{(-)}$  is the wave function of the system  $F = c + C = x + A$ ,  $\chi_{\mathbf{k}_{sF}}^{(-)}(\mathbf{r}_{ij})$  is the distorted wave of the system  $s + F$ ,  $\varphi_i$  is the bound state wave function of nucleus  $i$ ,  $\mathbf{r}_{ij}$  and  $\mathbf{k}_{ij}$  are the relative coordinate and relative momentum of nuclei  $i$  and  $j$ ,  $P = \{\mathbf{k}_{sF}, \mathbf{k}_{cC}\}$  is the six-dimensional momentum describing the three-body system  $s$ ,  $c$ , and  $C$ ,  $\Delta V_{sF} = V_{sF} - U_{sF}$ ,  $V_{sF} = V_{sc} + V_{sC} = V_{sx} + V_{sA}$  is the interaction potential of  $s$  and the system  $F$ , and  $U_{sF}$  is the optical potential.

The exact expression for the TH reaction amplitude, Equation (4), has been used as a starting point to derive the expression for the TH reaction amplitude proceeding through interfering resonances in the sub-system  $F$  (La Cognata et al. 2010c). If the direct coupling between the initial  $x + A$  and final  $c + C$  channels, which contributes dominantly to direct reactions but provides a negligible contribution to resonant reactions, is neglected, the wave function  $\Phi_F^{(-)}$  can be conveniently expressed using the spectral decomposition given by Equation (3.8.1) of Mahaux & Weidenmüller (1969). This leads to the shell model-based resonant  $R$ -matrix representation for  $\Phi_{F\alpha}^{(-)}$  in the channel  $\alpha$ , which is similar to the level decomposition for the wave function in the internal region in the  $R$ -matrix approach:

$$\Phi_{F\alpha}^{(-)} \approx \sum_{\nu, \tau=1}^N \tilde{V}_{\nu\alpha}(E_\alpha) [\mathbf{D}^{-1}]_{\nu\tau} \Phi_\tau. \quad (5)$$

Here,  $N$  is the number of the levels included,  $E_\alpha$  is the relative kinetic energy of nuclei in the channel  $\alpha$  (in the channel  $\alpha = c + C$ ,  $E_\alpha \equiv E_{cC}$ ), and  $\Phi_\tau$  is the bound state wave function describing the compound system  $F$  excited to the level  $\tau$ .  $\mathbf{D}_{\nu\tau}$  is the same level matrix as in the conventional  $R$ -matrix theory and is given by Equation (4.2.20b) of Mahaux & Weidenmüller (1969). It depends on the entry and exit channels reduced width amplitudes, energy levels, and energy shifts. This is an important step in the derivation of the resonant contribution to the TH reaction matrix element, as it entails that reduced width amplitudes and level energies can be obtained from the fitting

of the experimental THM cross section and used to deduce the  $A(x, c)C$  astrophysical factor. Finally,

$$\tilde{V}_{\nu\alpha}(E_\alpha) = \langle \chi_c^{(-)} \varphi_\alpha | \Delta V_\alpha | \Phi_\nu \rangle \quad (6)$$

is the resonant form factor for the decay of the resonance level  $\nu$  described by the compound state  $\Phi_\nu$  into the channel  $\alpha$  and  $\chi_\alpha^{(-)}$  is the distorted wave in the channel  $\alpha$ . The formal partial resonance width for the decay of this level into the channel  $\alpha$  is given by

$$\tilde{\Gamma}_{\nu\alpha}(E_\alpha) = 2\pi |\tilde{V}_{\nu\alpha}(E_\alpha)|^2. \quad (7)$$

In the  $R$ -matrix approach, the formal resonance width is related to the formal reduced width  $\gamma_{\nu\alpha}$  as  $\tilde{\Gamma}_{\nu\alpha}(E_\alpha) = 2P_l(E_\alpha, r_{0\alpha})\gamma_{\nu\alpha}^2$ , where  $P_l(E_\alpha, r_{0\alpha})$  is the barrier penetrability,  $l$  is the relative angular orbital momentum of nuclei in the channel  $\alpha$ , and  $r_{0\alpha}$  is the channel radius in the channel  $\alpha$ . The observable resonance width  $\Gamma_{\nu\alpha}$  for the decay of the resonance  $\nu$  into the channel  $\alpha$  is related to the formal one by (the Thomas approximation; Thomas 1951):

$$\Gamma_{\nu\alpha} = \frac{\tilde{\Gamma}_{\nu\alpha}(E_{R_{\nu\alpha}})}{1 + \sum_{\alpha'} \gamma_{\nu\alpha'}^2 \frac{dS_{\alpha'}}{dE_\alpha} \Big|_{E_\alpha=E_{R_{\nu\alpha}}}}, \quad (8)$$

provided that the boundary condition  $B_\alpha = S_\alpha(E_{R_{\nu\alpha}})$ , i.e., the energy of the  $\nu$ th level in the channel  $c$ , is  $E_{\nu\alpha} = E_{R_{\nu\alpha}}$ . Here,  $S_\alpha(E_\alpha)$  is the shift function in the channel  $\alpha$  and  $E_{R_{\nu\alpha}}$  is the  $\nu$ th resonance energy in the channel  $\alpha$ . Then, the TH reaction amplitude is

$$M^{(R)}(P, \mathbf{k}_{aA}) \approx \sum_{\nu, \tau=1}^N \tilde{V}_{\nu\alpha}(E_c) [\mathbf{D}^{-1}]_{\nu\tau} M_\tau(\mathbf{k}_{sF}, \mathbf{k}_{aA}), \quad (9)$$

where  $M_\tau(\mathbf{k}_{sF}, \mathbf{k}_{aA})$  is the exact amplitude for the direct transfer reaction  $a + A \rightarrow s + F_\tau$  populating the compound state  $F_\tau$  of the system  $F = x + A = c + C$ :

$$M_\tau(\mathbf{k}_{sF}, \mathbf{k}_{aA}) = \langle \chi_{sF}^{(-)} \Phi_\tau | \Delta V_{sF} | \Psi_i^{(+)} \rangle. \quad (10)$$

Equation (9) represents the generalization of the  $N$  level, two-channel  $R$ -matrix for the TH reaction, introduced by A. M. Mukhamedzhanov (Mukhamedzhanov et al. 2008; La Cognata et al. 2009, 2010c; Mukhamedzhanov 2011; La Cognata et al. 2011). As in the conventional  $R$ -matrix method, it contains the same level matrix  $\mathbf{D}_{\nu\tau}$ . But, in contrast to the conventional  $R$ -matrix amplitude for the  $x + A \rightarrow c + C$  resonant reaction, which contains the entry width amplitude  $\tilde{V}_{\tau xA}(E_{xA})$  (Lane & Thomas 1958), the generalized  $R$ -matrix amplitude contains the transfer reaction amplitude  $M_\tau(\mathbf{k}_{sF}, \mathbf{k}_{aA})$ , that is, the amplitude to populate the resonance state  $\tau$ . Such a transfer amplitude appears only in the numerator, while the level-matrix remains the same as in the case of the OES binary reactions, as was shown in the two-channel, two-level case (Mukhamedzhanov et al. 2008; La Cognata et al. 2009, 2010c, 2011; Mukhamedzhanov 2011). The transfer reaction amplitude accounts for the HOES nature of the TH transfer reaction. Since  $\tilde{\Gamma}_{\nu\alpha}(E_\alpha) = 2P_l(E_\alpha, r_{0\alpha})\gamma_{\nu\alpha}^2$ , the absence of the entry width amplitude  $\tilde{V}_{\tau xA}(E_{xA})$  implies that no Coulomb-barrier penetration factor suppresses the low-energy cross section, making it possible to extend measurements down to zero energy. However, the HOES feature of the TH cross section has to be taken into consideration in the data analysis.

In practical calculations, the exact  $M_\tau(\mathbf{k}_{sF}, \mathbf{k}_{aA})$  can be replaced by the DWBA one

$$M_\tau^{\text{DW}}(\mathbf{k}_{sF}, \mathbf{k}_{aA}) = \langle \chi_{sF}^{(-)} \Phi_\tau | \Delta V_{sF} | \varphi_a \varphi_A \chi_i^{(+)} \rangle. \quad (11)$$

The DWBA amplitude takes into account the rescattering of nuclei  $a$  and  $A$  in the initial state of the TH reaction and enters as a form factor into the TH resonant reaction amplitude. Correspondingly, for the amplitude of the TH reaction  $a + A \rightarrow c + C + s$ , we obtain from Equation (9) (the exit channel  $\alpha = c + C$ )

$$M^{(R)}(P, \mathbf{k}_{aA}) \approx \sum_{\nu, \tau=1}^N \tilde{V}_{\nu cC}(E_{cC}) [\mathbf{D}^{-1}]_{\nu\tau} M_\tau^{\text{DW}}(\mathbf{k}_{sF}, \mathbf{k}_{aA}). \quad (12)$$

Finally, the triple differential cross section for the TH process  $a + A \rightarrow s + c + C$  proceeding through interfering resonances is given by Mukhamedzhanov et al. (2008)

$$\frac{d^3\sigma}{dE_{cC} d\Omega_{\mathbf{k}_{cC}} d\Omega_{\mathbf{k}_{sF}}} = \frac{\mu_{cC} \mu_{sF} \mu_{aA}}{2\pi^5} \frac{k_{cC} k_{sF}}{k_{aA}} \frac{1}{\hat{J}_a \hat{J}_A} \times \left| \sum_{\nu, \tau=1}^N \tilde{V}_{\nu cC}(E_{cC}) [\mathbf{D}^{-1}]_{\nu\tau} M_\tau(\mathbf{k}_{sF}, \mathbf{k}_{aA}) \right|^2, \quad (13)$$

where  $\hat{J} = 2J + 1$  and  $J_i$  is the spin of particle  $i$ .

Under some simplifying hypothesis, the expression above can be written in a different form, explicitly showing the reduced widths  $\gamma$ . In the plane wave framework, assuming that the  $A(x, c)C$  reaction proceeds via isolated non-interfering resonances, the THM cross section takes the form (La Cognata et al. 2011, 2012; Mukhamedzhanov et al. 2008):

$$\frac{d^2\sigma}{dE_{xA} d\Omega_s} = \text{NF} \sum_i (2J_i + 1) \times \left| \frac{k_f(E_{xA})}{\mu_{cC}} \frac{\sqrt{2P_{l_i}(k_{cC} R_{cC})} M_i(p_{xA} R_{xA}) \gamma_{cC}^i \gamma_{xA}^i}{D_i(E_{xA})} \right|^2, \quad (14)$$

where NF is a normalization factor,  $k_f(E_{xA}) = \sqrt{2\mu_{cC}(E_{xA} + Q)}/\hbar$  ( $Q$  is the reaction  $Q$ -value),  $P_{l_i}$  is the penetration factor in the  $l_i$ -wave, and  $R_{xA}$  and  $R_{cC}$  are the channel radii.

$$M_i(p_{xA} R_{xA}) = \left[ (B_{xAi} - 1) j_{l_i}(\rho) - \rho \frac{\partial j_{l_i}(\rho)}{\partial \rho} \right]_{\rho=p_{xA} R_{xA}} \quad (15)$$

(Mukhamedzhanov 2011), where  $j_{l_i}(\rho)$  is the spherical Bessel function,  $p_{xA} = \sqrt{2\mu_{xA}(E_{xA} + B_{xs})}/\hbar$  ( $B_{xs}$  is the binding energy of the  $a = (xs)$  system), and  $B_{xAi}$  is an arbitrary boundary condition chosen as in La Cognata et al. (2010c, 2011, 2012) to yield the observable resonance parameters. Finally,  $D_i(E_{xA})$  is the standard  $R$ -matrix denominator in the case of one-level, two-channel  $R$ -matrix formulas (Lane & Thomas 1958).

In Equation (14), the same reduced widths appear as in the OES  $S(E)$ -factor, the only difference being the absence of any Coulomb or centrifugal penetration factor in the entrance channel. From the fitting of the experimental THM cross section, they can be obtained and used to deduce the OES astrophysical factor, which is not affected by either the electron screening or

the experimental energy resolution. In the plane wave approach, the HOES cross section is obtained in arbitrary units, making it necessary to introduce a normalization factor NF. As has been shown in several works (La Cognata et al. 2012, 2011, 2010c), normalization can be achieved by extending the indirect measurement to an energy region where directly measured resonances are available and scaling the deduced widths to match the values in the literature.

When dealing with sub-threshold resonances, the equations above have to be modified as for bound states since penetrability is zero at negative energies, but the shift function can still be defined as the logarithmic derivative of the Whittaker function (Thompson & Nunes 2009). Accordingly, the true resonance position, namely the energy where the  $S$ -matrix has a pole, can be obtained by solving the implicit equation  $E_R = e_p - \gamma^2(S(E_R) - a\beta)$ , which calculates the difference between the  $R$ -matrix pole energy and the actual bound state, where  $e_p$  is the  $R$ -matrix pole,  $a$  is the  $R$ -matrix radius, and  $\beta$  is an arbitrary boundary condition parameter. In each spin and parity channel  $J_{\text{tot}}^\pi$ , we can choose  $\beta$  so that  $S^0(E) = 0$  at some preferred energy  $E$ . If  $\phi(r)$  is the true (single-channel) bound state and  $\beta$  chosen as  $\beta = \phi'/\phi$  at  $r = a$  from the “natural boundary condition,” then  $S^0 = 0$  at the bound state. The application of this natural boundary condition to a specific sub-threshold state, whose energy is already known from the literature, yields the observable resonance parameters for this sub-threshold state. The  $R$ -matrix eigenfunction  $w(r)$  is proportional to  $\phi(r)$  inside the  $R$ -matrix radius  $a$ :  $\phi(r) = Aw(r)$ , where  $A^2 = 1 - \int_a^\infty |\phi(r)|^2 dr$  reflects the different normalization requirements. Outside the  $R$ -matrix radius, the Whittaker function  $W(r)$  describes the asymptotic behavior of the bound state wave function of two charged particles and the ANC defines the amplitude of its tail, namely, the ANC value  $C$  is the coefficient in  $\phi(r) = CW(r)$  for the Whittaker function (Mukhamedzhanov et al. 1995; Mukhamedzhanov & Tribble 1999). The reduced width is therefore (Thompson & Nunes 2009):

$$\gamma^2 = \frac{\hbar^2}{2\mu a} \frac{C^2 W(a)^2}{1 - C^2 \int_a^\infty |W(r)|^2 dr}. \quad (16)$$

For deeply bound states  $A \sim 1$  and then we have the proportionality  $\gamma^2 \propto C^2$ , but the integral in the denominator may become important for weakly bound or halo states (Mukhamedzhanov & Tribble 1999; Thompson & Nunes 2009). Therefore, from the THM measurement of a sub-threshold state, yielding the reduced widths  $\gamma$ , the ANC can be deduced, clearly showing the deep connection of the two indirect approaches (La Cognata et al. 2012).

However, the THM approach to the extraction of the ANC presents some advantages, which will be discussed in more detail in the forthcoming sections. In the standard approach, the angular distributions of transfer reactions are usually measured and fit in different theoretical frameworks, to evaluate the sensitivity of the deduced ANC on the optical potentials used in the calculations. As shown in previous sections, ambiguities on the reaction mechanism, transfer versus compound nucleus, for instance, might arise introducing systematic errors of poorly known size. Moreover, background reactions might determine an inaccurate estimate of the true counting rate if incorrectly subtracted. In contrast, three-body kinematics make it possible to use a number of kinetic tests leading to an unambiguous identification of the reaction channel, allowing us to separate the  $A(a, cC)s$  channel from background reactions (Spitaleri

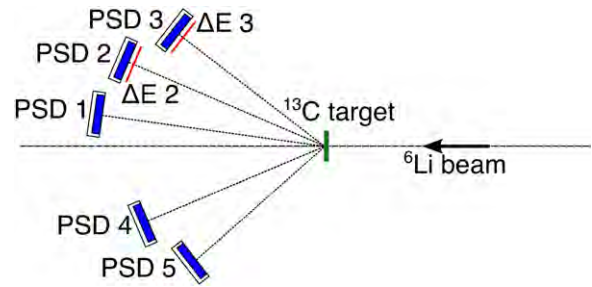


**Figure 2.** Sketch of the experimental setup. The 99%  $^{13}\text{C}$  enriched target is shown in green and PSD 1–5 are shown in the blue boxes. Red segments are used for  $\Delta E$  detectors. The beam axis is highlighted by the dashed line, while the beam direction is marked by the arrow.

(A color version of this figure is available in the online journal.)

et al. 2011) and to single out the requested branch (e.g., the population of particles  $C$  in the ground state). A necessary condition for the application of the THM is the evaluation of the presence of the QF mechanism, which has to be disentangled from other competing reaction mechanisms. Because of the clear signature of the QF process, this reaction mechanism can be unambiguously singled out from the  $A(a, cC)s$  reaction yield.

In this work, we exhaustively discuss the indirect investigation of the  $^{13}\text{C}(\alpha, n)^{16}\text{O}$  reaction over a broad energy range, from 1.2 MeV down to about  $-300$  keV. We extend the THM to the analysis of sub-threshold resonances and we extract the ANC  $\tilde{C}_{\alpha^{13}\text{C}}^{17\text{O}(1/2^+)}$  characterizing the sub-threshold resonance from THM data. Moreover, the neutron partial width  $\Gamma_n$  is also inferred by means of Equation (14) and both parameters will be used to determine the contribution of the  $-3$  keV resonance to the  $^{13}\text{C}(\alpha, n)^{16}\text{O}$  reaction rate.

#### 4. THE $^{13}\text{C}(^6\text{Li}, n^{16}\text{O})d$ EXPERIMENT

In this work, the  $^{13}\text{C}(\alpha, n)^{16}\text{O}$  astrophysical factor is deduced from the  $^{13}\text{C}(^6\text{Li}, n^{16}\text{O})d$  cross section. The experiment was performed at the Florida State University Tandem-LINAC facility, which delivered a  $E_b = 7.82$  MeV, 1 mm spot  $^6\text{Li}$  beam impinging onto 99%  $^{13}\text{C}$  enriched foils, whose thicknesses  $d_i$  were chosen to be  $53 \mu\text{g cm}^{-2}$  and  $107 \mu\text{g cm}^{-2}$ . We use  $^6\text{Li}$ , which has a well known  $\alpha + d$  structure, as the TH nucleus. Therefore, the TH reaction process proceeds through the transfer of an  $\alpha$ -particle off  $^6\text{Li}$  to  $^{13}\text{C}$ , while  $d$  is emitted without interacting, assuming a QF reaction mechanism.  $^{16}\text{O}$  from the  $^{13}\text{C}(\alpha, n)^{16}\text{O}$  sub-reaction and deuterons are detected, to maximize the detection efficiency and reduce systematic uncertainties. This is one of the advantages of the THM approach; since the kinematic variables for all of the ejectiles can be determined from the energies and angles of the emission of two particles, one can choose the ones easiest to detect that show the best resolution or introduce the smallest systematic errors (see Tumino et al. 2011).

A sketch of the experimental setup is shown in Figure 2. It consisted of five  $5 \times 1 \text{ cm}^2$  position-sensitive silicon detectors, hereafter called PSDs 1–5, with energy and position resolutions of 0.5% and  $0.3 \mu\text{m}$ , respectively. PSDs 1–3, covering the  $3^\circ$ – $44^\circ$  angular range, were devoted to deuteron detection; in particular, PSD 1 was shielded by a  $20 \mu\text{m}$  Al foil to stop particles with  $Z > 2$ , while  $20 \mu\text{m}$  silicon  $\Delta E$  detectors were placed in front of PSDs 2–3 for particle identification (hence the names  $\Delta E2$  and  $\Delta E3$  in Figure 2).  $\Delta E$  detectors introduced

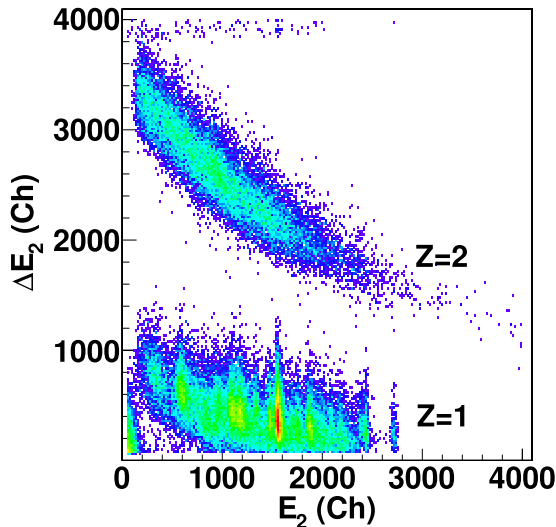


**Figure 3.**  $\Delta E$ - $E$  two-dimensional spectrum for the  $\Delta E2$ -PSD 2 detector couple. Labels are used to mark the loci corresponding to atomic numbers  $Z = 1$  and  $Z = 2$ .  $\Delta E_2$  and  $E_2$  (that is, the energy signals from  $\Delta E2$  and PSD 2, respectively) are given in the analog-to-digital converter channels.

(A color version of this figure is available in the online journal.)

a  $\sim 1.47$  MeV threshold while the Al degrader introduced a slightly larger threshold of  $\sim 1.54$  MeV for deuteron detection. PSDs 4–5 covered the  $17^\circ$ – $45^\circ$  angular range, on the opposite side of the beam direction, to detect  $^{16}\text{O}$  nuclei emitted in coincidence. In this way, a large part of the QF kinematics was covered and no significant detection thresholds were introduced.

Since the momentum distribution for the  $d - \alpha$  system has a maximum at  $p_d = 0$  MeV  $c^{-1}$ , the bulk of the QF contribution for deuteron breakup corresponds to forward deuteron emission angles. This warrants the need to cover small angles (as low as  $3^\circ$  in the laboratory system), in order to maximize the expected QF contribution to the total reaction yield. In turn, no particle identification was possible for particles impinging on PSD 1; however, deuteron events were singled out from reaction kinematics. A similar approach was used to pick out  $^{16}\text{O}$  nuclides hitting PSDs 4–5. More details on the  $^{13}\text{C}(^6\text{Li}, n^{16}\text{O})d$  channel selection are given in the following subsection.

Energies and emission angles of the detected deuterons and the energies of  $^{16}\text{O}$  nuclei were used in the subsequent analysis to enhance the  $^{13}\text{C} - \alpha$  relative energy resolution. The trigger of the acquisition system was the coincidental detection of a particle in PSD 1–3 and one in PSDs 4–5, using a time-to-amplitude converter (TAC). The energy and position signals of the PSDs were processed by standard electronics together with the TAC signal for each coincidental event and sent to the acquisition system for on-line monitoring and data storage for off-line processing.

At the initial stage of the measurement, masks with a number of equally spaced slits were placed in front of each PSD to perform the position calibration. The angle of each slit with respect to the beam direction was measured by means of an optical system, making it possible to establish a correspondence between the position signal from the PSDs and the detection angle of the impinging particles. Energy calibration was performed by means of a  $^{228}\text{Th}$  (6 peak)  $\alpha$ -source and by using a  $^6\text{Li}$  beam scattered off  $^{197}\text{Au}$  and  $^{12}\text{C}$ , as well as  $\alpha$  particles emitted in the  $^{12}\text{C}(^6\text{Li}, \alpha)^{14}\text{N}$  reaction. The total kinetic energy of the detected particles was reconstructed

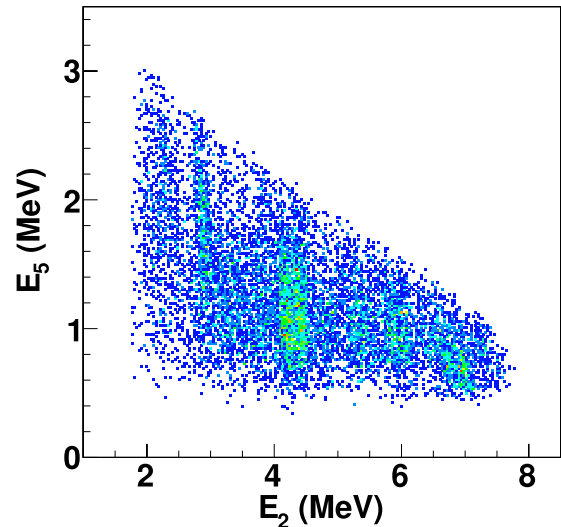


**Figure 4.**  $E_5$  vs.  $E_2$  correlation plot.  $E_5$  and  $E_2$  are the energies of the particles detected in PSDs 2 and 5, respectively, including the energy loss in dead layers and in the  $\Delta E$  detector.

(A color version of this figure is available in the online journal.)

off-line, taking into account the energy loss in the target and in the dead layers of the detectors.

#### 4.1. Reaction Channel Selection

After detector energy and position calibration, the  $^{13}\text{C}(^6\text{Li}, n^{16}\text{O})d$  channel was selected by using the standard approach described in La Cognata et al. (2007, 2010a), for instance. Indeed, at 7.82 MeV, the beam energy of the  $^6\text{Li} + ^{13}\text{C}$  interaction can lead to 20 different exit channels, while impurities in the target ( $^{12}\text{C}$  already in the target and from carbon built up during the experiment; H and O from moisture) might contribute more, although less populated, open channels. The reaction channel selection is therefore a pivotal step in the application of the THM.

A coincidental detection of reaction products triggered by a TAC drastically reduces the contribution of reaction channels other than the  $n + ^{16}\text{O} + d$  one that is recorded for the subsequent data analysis. Furthermore, a gate is introduced in the TAC spectrum to remove spurious coincidences. The resulting recorded  $\Delta E$ - $E$  spectrum is shown in Figure 3 for the  $\Delta E2$ -PSD 2 detector couple. The amplification of the  $\Delta E_2$  signal was set to record events with  $Z \leq 2$ . Figure 3 clearly shows two regions, corresponding to particles with atomic numbers 1 and 2. The position of the  $Z = 2$  locus was checked during the calibration stage by detecting  $\alpha$  particles from the  $^{228}\text{Th}$  source. It is mostly populated by  $\alpha$  particles emitted following direct  $^6\text{Li}$  breakup. The  $Z = 1$  region was selected by means of a graphical cut for the further analysis. As discussed above, no  $\Delta E$  detectors were placed in front of PSDs 1, 4, and –5. Therefore, further studies are needed to single out the  $^{13}\text{C}(^6\text{Li}, n^{16}\text{O})d$  reaction.

It is well known that particles from reactions with three nuclei in the exit channel have kinetic energies that are correlated through energy and momentum conservation laws (see, for instance, Ohlsen 1965). By comparing the experimental kinematic locus with the results of a Monte Carlo simulation taking into account detection thresholds, energy losses, and the kinematics of the TH reaction, evidence of events from the  $^{13}\text{C}(^6\text{Li}, n^{16}\text{O})d$  reaction and background processes can be found. Figure 4 shows

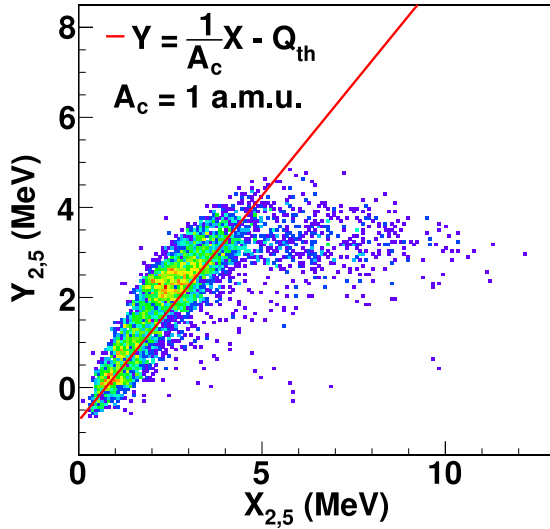
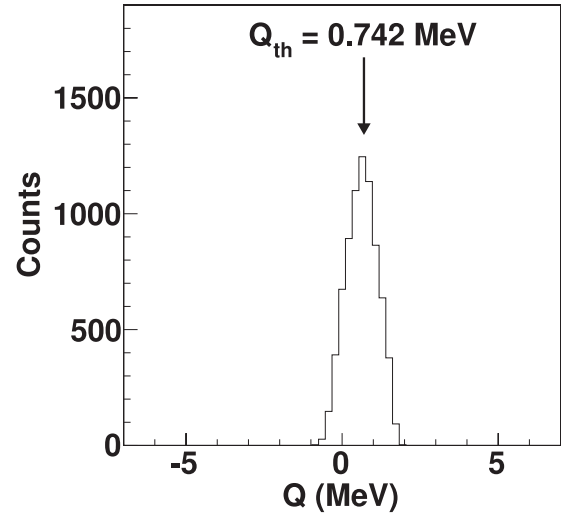


**Figure 5.** Identification of the undetected particle according to the procedure of Costanzo et al. (1990), applied to the PSD 2 and 5 coincidence. According to our definition of the THM reaction, namely  $A(a, cC)s$ , the undetected neutron is identified with the letter  $c$ . On the horizontal axis, the quantity  $X = p_c^2/2u$  is given;  $u$  is a unit mass in a.m.u. and  $p_c$  is the momentum of the undetected particle, while the difference  $Y = E_b - E_2 - E_5$  is shown on the vertical axis. The two-dimensional histogram is obtained by selecting  $Z = 1$  events in Figure 3. The red line is calculated assuming  $A_c = 1$  and a theoretical  $Q_{\text{th}} = 0.742$  MeV. Events gather along this line, attesting that they are emitted in reactions where a particle of unit mass is emitted, with a  $Q$ -value in agreement with the theoretical one.

(A color version of this figure is available in the online journal.)

the correlation plot for PSDs 2 and 5. The energies of the particles detected in these detectors were reconstructed by summing the simulated energy loss in the dead layers and the energy loss measured in the  $\Delta E$  detector. Figure 4 shows the detection thresholds in the actual measurement,  $\sim 1.7$  MeV for PSD 2 and  $\sim 0.5$  MeV for PSD 5, slightly larger than the calculated values owing to the presence of dead layers and electronic thresholds. A good agreement is found between the simulated two-dimensional plot and the experimental kinematic locus, suggesting that only a small background might contribute, besides the  $^{13}\text{C}(^6\text{Li}, n^{16}\text{O})d$  reaction. A very interesting feature seen in Figure 4 is the occurrence of regions where a large number of counts is present, for fixed energies in PSD 2 (that is, for fixed deuteron energies). As we will discuss later, this is a hint of the population of  $^{17}\text{O}$  states. A similar approach has been applied to the other couples of coincidence detectors.

In this experiment, only two of the three emitted particles were detected. Though this proved to be a great advantage, as only charged particles were collected, the overlapping different kinematic loci in the same phase-space region, corresponding to reactions having different undetected particles, might be responsible for that background that has to be identified and subtracted from the total reaction yield. Indeed, Figure 4 cannot be used to disentangle such contributions as only a single locus appears. Costanzo et al. (1990) introduced a very useful test that allowed for the identification of the mass of the undetected particle and for the extraction of the experimental  $Q$ -value for the selected events. For this purpose, for the events belonging to the  $Z = 1$  region of Figure 3, the difference  $Y = E_b - E_2 - E_5$  between the beam energy and the emitted particle energies measured in PSDs 2 and 5 was calculated. Here, we focus on the coincidence of PSDs 2 and 5, as in



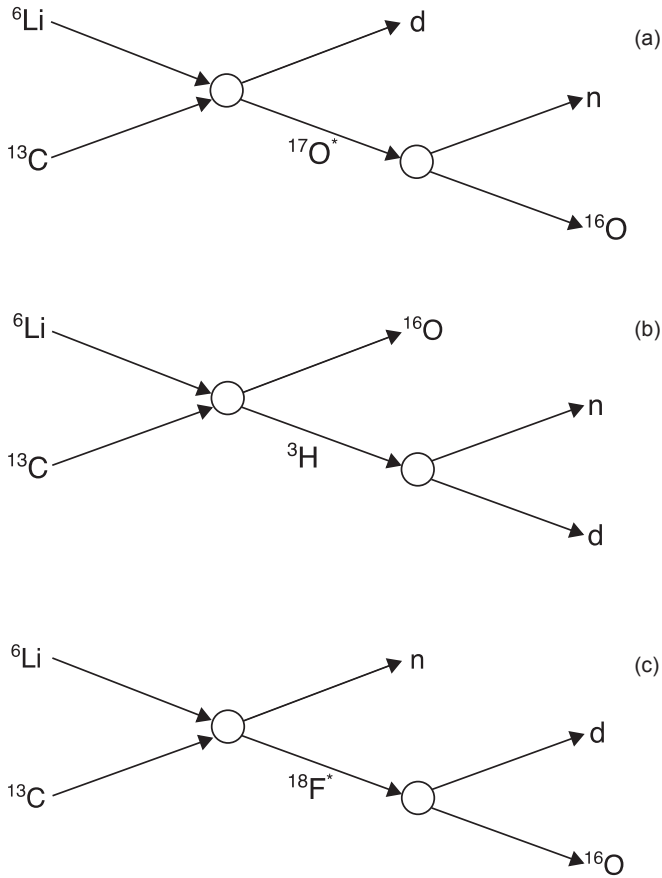
**Figure 6.** Experimental  $Q$ -value spectrum, for the events belonging to the  $Z = 1$  locus in Figure 3 and situated along the red line in Figure 5. A single peak shows up, centered at the theoretical  $Q_{\text{th}} = 0.742$  MeV (marked by an arrow).

Figure 4, but similar considerations can be drawn for other detector couples. The quantity  $Y$  defined above is plotted against the variable  $X = p_c^2/2u$ , where  $p_c$  is the momentum of the undetected particle (a neutron, if the recorded event corresponds to the  $^{13}\text{C}(^6\text{Li}, n^{16}\text{O})d$  process) and  $u$  is a unit mass in a.m.u. Since  $p_c$  is deduced from the energies and emission angles of particles  $s$  and  $C$  (deuteron and  $^{16}\text{O}$ ) by applying the momentum conservation equation,  $X$  is independent of the mass of the fragment  $c$ . Therefore, analysis of the  $Y$  versus  $X$  diagram can reveal the mass of the undetected particle as events produced in the  $^{13}\text{C}(^6\text{Li}, n^{16}\text{O})d$  reaction should gather along a line described by

$$Y = \frac{1}{A_c} X - Q_{\text{th}}, \quad (17)$$

which is deduced from the energy conservation equation. The  $Y$  versus  $X$  diagram for the PSD 2 and 5 detector couple is shown in Figure 5, together with a red line obtained from Equation (17) by setting  $A_c = 1$  and a  $Q_{\text{th}} = 0.742$  MeV. Most of events clearly assemble along this line, allowing us to infer the mass of  $c$  with no need for a measurement. We can state that the experimental  $Q$ -value agrees with the one expected on the basis of the masses of the particles involved in the  $^{13}\text{C}(^6\text{Li}, n^{16}\text{O})d$  reaction. However, Figure 5 shows that some contaminating process also contributes to the coincidence yield, which has been discarded by introducing a graphical cut encompassing only those events located along the red line.

To evaluate the effectiveness of the background rejection procedure outlined so far, as well as to check the accuracy of the performed calibration, the experimental  $Q$ -value spectrum was deduced for those events satisfying the  $Z = 1$  condition in Figure 3 and disposed along the red line in Figure 5. The result is shown in Figure 6. A single peak is apparent, centered at an energy of about 0.742 MeV, corresponding to the theoretical  $Q$ -value, demonstrating that no channel other than the  $^{13}\text{C}(^6\text{Li}, n^{16}\text{O})d$  is present and that the detector calibration introduces no systematic error. Similar results are deduced from the other coincidence detector pairs. In the following, the data analysis is restricted to such events.



**Figure 7.** Sketch of possible SD processes feeding the  $n + {}^{16}\text{O} + d$  exit channel. The empty circle is used to emphasize that, in general, the first reaction in the sequence cannot be described as direct.

#### 4.2. Investigation of the Reaction Mechanisms Contributing to the ${}^{13}\text{C}({}^6\text{Li}, n){}^{16}\text{O}d$ Yield

The presence of QF mechanism was investigated, since Equation (14) can be applied to QF data only in order to extract the reduced  $\gamma$ -widths. In other words, it is necessary to establish whether the outgoing deuteron acted as a spectator in the  ${}^{13}\text{C} - \alpha$  interaction. Therefore, reaction dynamics were studied to select those regions where the QF mechanism is dominant and can be separated from possible direct breakup (DBU) or sequential decay (SD) reaction mechanisms. In fact, the same exit channel selected by investigating the reaction kinematics can be fed through different reaction mechanisms. SD processes are especially critical as they proceed through the population of compound systems, possibly leading to resonances dominating the coincidence yield and hiding the QF contribution.

In Figure 7, some examples of possible SD mechanisms leading to the population of the  $n + {}^{16}\text{O} + d$  exit channel are juxtaposed. While in Figure 1 the spectator deuteron (particle  $s$ ) flies away after  ${}^6\text{Li}$  breakup without influencing the  ${}^{17}\text{O} \rightarrow n + {}^{16}\text{O}$  decay, here it can either be emitted in the  ${}^{13}\text{C}({}^6\text{Li}, d){}^{17}\text{O}$  compound nucleus reaction (diagram (a) in Figure 7) or by  ${}^3\text{H}$  or  ${}^{18}\text{F}$  intermediate systems, excited above the deuteron emission threshold (diagrams (b) and (c) in Figure 7). In the last two cases, the  $n - d$  or  $d - {}^{16}\text{O}$  relative energy spectra should reveal peaks correlated with  ${}^3\text{H}$  or  ${}^{18}\text{F}$  states. Therefore, the occurrence of SD processes taking place by  ${}^3\text{H}$  or  ${}^{18}\text{F}$  decay can be discovered by inspecting the  $E_{n-d}$  and the  $E_{d-{}^{16}\text{O}}$  relative energy spectra, respectively.

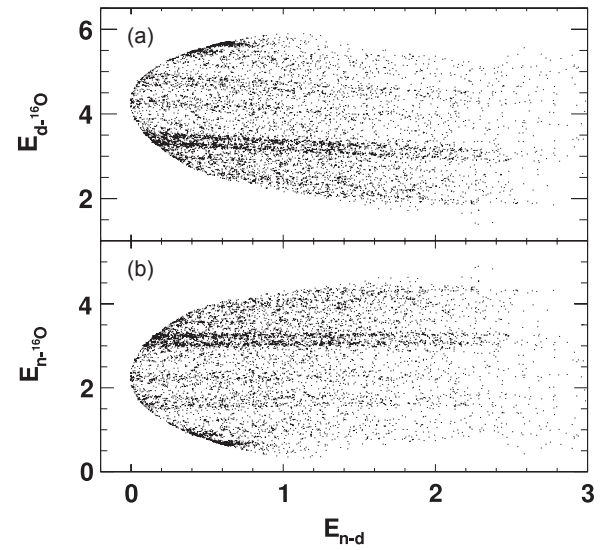


**Figure 8.** Energy correlation two-dimensional spectra.  $E_{d-{}^{16}\text{O}}$  and  $E_{n-{}^{16}\text{O}}$  (the  $d - {}^{16}\text{O}$  and  $n - {}^{16}\text{O}$  relative energies, respectively), are graphed against the  $n - d$  relative energy,  $E_{n-d}$ . Horizontal loci in the lower panel correspond to  ${}^{17}\text{O}$  excited states. No additional loci are apparent, i.e., no sequential decay process contributes.

Two-dimensional relative energy plots for any two of the three final particles were then reconstructed. Relative energies  $E_{d-{}^{16}\text{O}}$  and  $E_{n-{}^{16}\text{O}}$  are given in Figure 8 as a function of  $E_{n-d}$  relative energy for the PSD 2 and 5 coincidence (upper and lower panels, respectively). No vertical locus shows up, corresponding to the formation of  ${}^3\text{H}$ , as it is expected since triton has no excited states. In the upper panel, no horizontal loci are present, making us confident that the  ${}^{13}\text{C}({}^6\text{Li}, n){}^{16}\text{O}d$  reaction does not proceed through the SD process given in Figure 7(c), or at least that the  ${}^{18}\text{F}$  sequential decay is a less favored process, in the examined phase-space region. Similar results are obtained for the other coincidence detector couples.

Though no contribution from  ${}^{18}\text{F}$  decay feeds the experimental relative energy spectra,  ${}^{17}\text{O}$  levels clearly emerge. This fact is shown by the horizontal loci apparent in the lower panel of Figure 8. From the comparison with the compilation of Tilley et al. (1993), these enhancements in the reaction yield should be attributed to  ${}^{17}\text{O}$  states whose excitation energies range from the  ${}^{17}\text{O} \rightarrow n + {}^{16}\text{O}$  threshold (4.144 MeV) up to about 8 MeV. In particular, the  $E_{n-{}^{16}\text{O}}$  versus  $E_{n-d}$  plot (Figure 8(b)) displays the contribution of the  ${}^{17}\text{O}$  states at 6.356 MeV ( $J^\pi = 1/2^+$ ), 7.165 MeV ( $J^\pi = 5/2^-$ ), 7.248 MeV ( $J^\pi = 3/2^+$ ), 7.378 MeV ( $J^\pi = 5/2^+$ ), and 7.381 MeV ( $J^\pi = 5/2^-$ ), affecting the astrophysical factor of the  ${}^{13}\text{C}(\alpha, n){}^{16}\text{O}$  in the 0–1 MeV energy range.

It is important to note that  ${}^{17}\text{O}$  levels can be populated through a QF and/or a SD process, as the  ${}^{17}\text{O}$  formation can take place through the diagram of Figure 1 or through diagram (a) of Figure 7. Thus, the occurrence of sequential mechanisms in the  $n - {}^{16}\text{O}$  channel cannot be ruled out by studying the relative energy correlation plots only. A way to discriminate between SD and QF events is through experimental study of the deuteron momentum spectrum (Spitaleri et al. 2011; Pizzone et al. 2005, 2009; La Cognata et al. 2010a, 2010b). If  ${}^6\text{Li}$  breakup process is direct, as requested for the application of the THM, the deuteron momentum distribution keeps the same shape as inside  ${}^6\text{Li}$ . The agreement between the shape of the  ${}^6\text{Li}$  momentum distribution and the experimental one is then compelling evidence for the occurrence of the QF mechanism. In particular, since the  $\alpha - d$

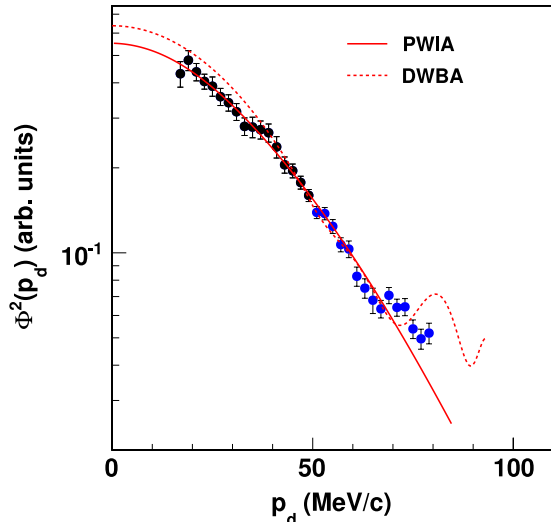


**Figure 9.** Experimental deuteron momentum spectrum (black and blue dots, for the PSD 1 and 5 and 2 and 5 coincidence couples, respectively), contrasted with the theoretical deuteron momentum distributions inside  ${}^6\text{Li}$ . In the PWIA approach (solid red line), this is taken from Pizzone et al. (2009); in the DWBA (dotted red line), the deuteron momentum spectrum is evaluated by means of the FRESKO code (Thompson 1988). Normalization was left as a free fitting parameter. Only statistical errors are displayed.

(A color version of this figure is available in the online journal.)

motion inside  ${}^6\text{Li}$  takes place in an s-wave, the momentum distribution of the  $\alpha - d$  system inside  ${}^6\text{Li}$  should have a maximum at  $p_d = 0 \text{ MeV c}^{-1}$  (in the  $\alpha - d$  center-of-mass system). Therefore, an enhancement of the cross section close to zero deuteron momentum is a necessary condition for the occurrence of the QF mechanism.

The  $p_d$  experimental spectrum, converted to the  ${}^6\text{Li}$  center of mass (as the projectile nucleus undergoes breakup), is reported in arbitrary units in Figure 9 as solid circles, blue for the PSD 2 and 5 coincidence couple and black for the 1 and 5 one. The procedure to extract the experimental momentum distribution is discussed at length elsewhere (La Cognata et al. 2010a, 2010b; Spitaleri et al. 2004; Lamia et al. 2012). It is worth noting that phase-space effects were accounted for by dividing the coincidence yield by the result of a Monte Carlo simulation, accounting for the experimental setup, the covered angular ranges in the experiment, and the detection thresholds. In addition, the effect of resonances in the  $E_{n-{}^{16}\text{O}}$  spectrum was corrected for, as the rapid increase in the reaction yield due to the population of  ${}^{17}\text{O}$  states would introduce distortion in the  $p_d$  experimental spectrum. For this purpose, the entire deuteron momentum spectrum was divided in a number of intervals, spanning  $E_{n-{}^{16}\text{O}}$  regions where the reaction yield could be assumed to be constant, with overlapping regions to ensure relative normalization. From Figure 9, it turns out that a 20–80  $\text{MeV c}^{-1}d$ -momentum range was covered in the present experimental setup, a region very sensitive to the shape of the momentum distribution, thus allowing for an accurate test of the occurrence of the QF reaction mechanism. The experimental  ${}^6\text{Li}$  momentum distribution is compared with the theoretical ones,  $|\Phi(p_d)|^2$ , reported as red lines in Figure 9. In the plane wave impulse approximation (PWIA), this is calculated as discussed in Pizzone et al. (2009). The resulting function (solid red line), matches well with the experimental  $d - \alpha$  momentum distribution, after adjusting the  $N$  NFs to the data. This indicates that the  ${}^{13}\text{C}({}^6\text{Li}, n){}^{16}\text{O}$  reaction proceeds through direct  $\alpha$ -transfer in the phase space region

under examination in the present work, allowing us to apply the THM to extract the astrophysical factor of the  ${}^{13}\text{C}(\alpha, n){}^{16}\text{O}$  reaction. The agreement also corroborates the use of the PWIA as no distortions are needed to describe the transfer process (La Cognata et al. 2010b).

To check whether the simple PWIA approach gives an accurate description of the  $\alpha - d$  relative momentum distribution, the DWBA distribution was evaluated by means of the FRESKO computer code (Thompson 1988) and reported in Figure 9 as a red dotted line. The procedure we followed is similar to the one outlined in La Cognata et al. (2010b). The theoretical DWBA momentum distribution has been scaled to the experimental data as these are given in arbitrary units. In the calculation, optical potential parameters from Johnson et al. (2006) have been adopted, with no adjustment. From the comparison, we can state that a good agreement between the PWIA and DWBA distributions is present for a deuteron momentum  $p_d < 75 \text{ MeV c}^{-1}$ , which is within the experimental uncertainties (including only the statistical error, in the case of Figure 9). This confirms that the PWIA approach constitutes a viable tool to extract the resonance parameters for the  ${}^{13}\text{C}(\alpha, n){}^{16}\text{O}$  reaction and that distortions play a minor role. In fact, according to the resonant THM outlined in the beginning, the  $2 \rightarrow 3$  cross section used to extract the resonance parameters is integrated over  $p_d$ ; thus, distortions would provide a contribution as small as 3% to the overall error budget in the 50–80  $\text{MeV c}^{-1}$  range spanned in this measurement (as discussed in the next section). Similarly, the PWIA momentum distribution deviates from the data trend by 3% in the same range. Such systematic effects will add up to the total errors budget.

## 5. EXTRACTING THE CROSS SECTION OF THE ${}^{13}\text{C}({}^6\text{Li}, n){}^{16}\text{O}$ QF REACTION

From the analysis of the relative energy spectra, it turns out that clear evidence of the population of  ${}^{17}\text{O}$  levels is present only in the PSD 2 and 5 coincidence couple, as is apparent from Figure 8. Therefore, we focus on this coincidence couple in the following. Figure 10 shows the QF coincidence yield spectra obtained by selecting the  ${}^{13}\text{C}({}^6\text{Li}, n){}^{16}\text{O}$  reaction channel as discussed in Section 4.1 and focusing on the  $50 < p_d < 80 \text{ MeV c}^{-1}$  deuteron momentum range (in the  ${}^6\text{Li}$  center-of-mass system) to single out the QF contribution to the reaction yield. They are plotted as a function of the  ${}^{13}\text{C} - \alpha$  relative energy, calculated through Equation (1), which can be cast in the form:

$$E_{\text{c.m.}} = E_{n-{}^{16}\text{O}} - Q_2, \quad (18)$$

where  $E_{n-{}^{16}\text{O}}$  is the relative energy between the outgoing neutron and  ${}^{16}\text{O}$  and  $Q_2 = 2.216 \text{ MeV}$  is the Q-value of the  ${}^{13}\text{C}(\alpha, n){}^{16}\text{O}$  reaction. In panel (a), the experimental cross section determined with the thinner target,  $d_t = 53 \mu\text{g cm}^{-2}$ , is presented, while data taken with the thicker target,  $d_t = 107 \mu\text{g cm}^{-2}$ , are shown in panel (b). The experimental spectra are corrected for phase space effects by dividing the coincidence yield by the simulated  ${}^{13}\text{C} - \alpha$  relative energy spectra, accounting for reaction kinematics, energy thresholds, and analysis cuts used to disentangle the QF contribution, modulated by the  $\alpha - d$  momentum distribution inside  ${}^6\text{Li}$ . Because of the good agreement with the experimental momentum distribution and the DWBA distribution, the PWIA distribution (Pizzone et al. 2009) was introduced into calculations. In Figure 10, vertical error bars include statistical errors only, while the horizontal error bars show the width of the integration bin.

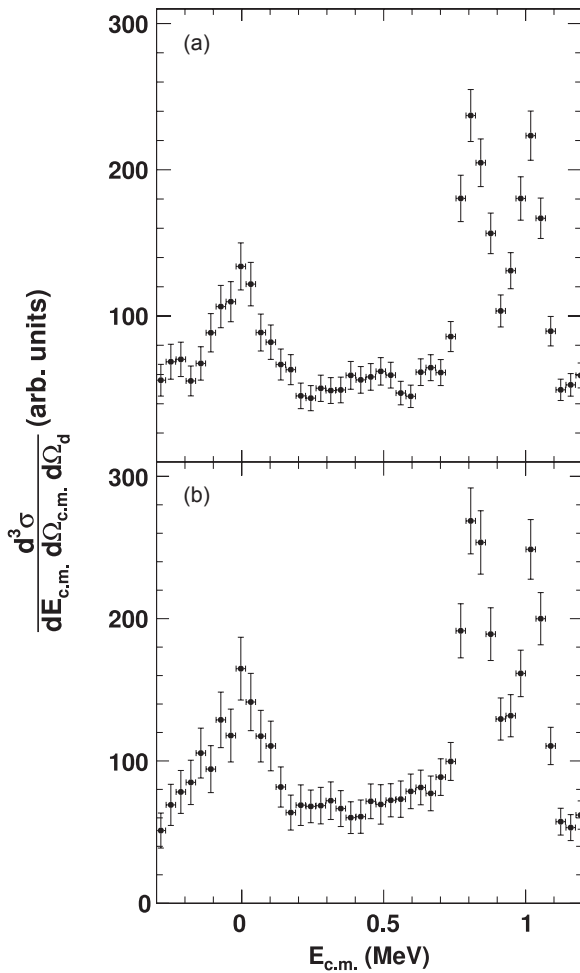


**Figure 10.** Normalized coincidence yield of the  $^{13}\text{C}(^6\text{Li}, n^{16}\text{O})d$  THM reaction, as a function of  $^{13}\text{C} - \alpha$  relative energy, obtained by introducing the analysis cuts discussed in the text. The QF condition has been enforced by selecting the  $50 \text{ MeV } c^{-1} < p_d < 80 \text{ MeV } c^{-1}$  deuteron momentum range. The vertical error bars include the statistical uncertainty only. The horizontal error bars highlight the size of the integration bin. In panel (a), data obtained using the  $53 \mu\text{g cm}^{-2}$   $^{13}\text{C}$  target are displayed; in panel (b), the cross section measured with the  $107 \mu\text{g cm}^{-2}$   $^{13}\text{C}$  target is shown.

The two datasets (acquired with thin and thick targets, respectively) were analyzed separately as different systematic errors might be present, linked to possible different amounts of impurities or surface inhomogeneities, for instance. It is important to note that the experimental THM cross section in panel (a) (corresponding to  $d_t = 53 \mu\text{g cm}^{-2}$ ) is the same as the one reported in Figure 1 of La Cognata et al. (2012), before background subtraction and angular distribution integration. Indeed, one of the purposes of the present work is to perform an improved data analysis, in addition to discussing in detail the experimental and the data reduction procedures. This is accomplished by a more thorough investigation of the conceivable sources of systematic errors and by increasing statistics to lower the contribution of statistical uncertainty to the overall error budget.

From the inspection of the upper and lower panels of Figure 10, it is apparent that the normalized yield spectra are in good agreement with each other within uncertainties, the only difference being due to the total statistics, which are lower in the spectrum visible in panel (b). This is what should be expected since the kinematic variable mostly affecting the  $E_{c.m.}$  energy resolution is the angle of emission of  $^{16}\text{O}$ , as a

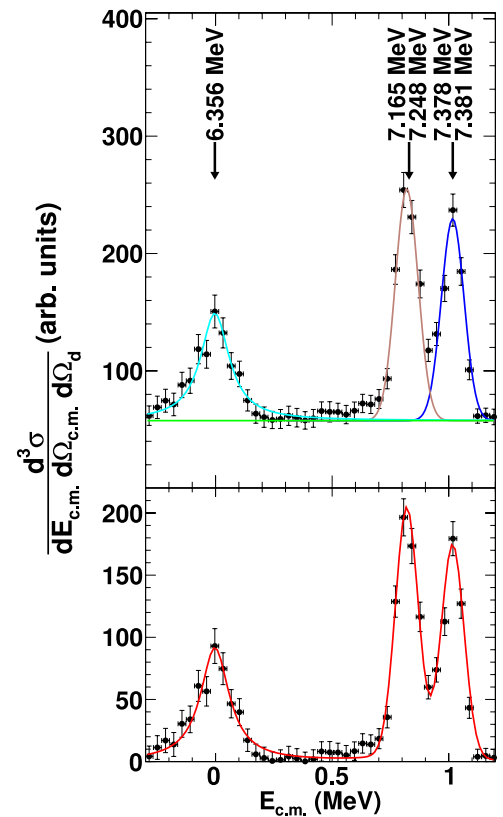


**Figure 11.** Upper panel: weighed sum of the  $E_{c.m.}$  spectra in Figure 10. A multi-Gaussian fit has been used to disentangle the contribution of the resonances, marked by arrows, to the coincidence yield. The contributions of the resonances at  $-3$  keV,  $806$  keV, and  $1019$  keV are described by light blue, brown, and blue curves, respectively. The  $889$  keV and  $1022$  keV resonance contribution to the THM cross section is negligible. A green straight line is used to denote the flat background. Lower panel: background subtracted QF reaction yield as a function of  $^{13}\text{C} - \alpha$  relative energy. Vertical error bars include statistical and background subtraction uncertainties. The red line represents the sum of the contributions of the resonances identified in the upper panel.

(A color version of this figure is available in the online journal.)

consequence of straggling in the target. Indeed, the relative energy resolution is fixed by the beam spot size and divergence, the energy and angular straggling in the  $\Delta E$  detectors, the Al foil, the target and dead layers, and the PSD intrinsic angular and energy resolutions. Since the calculation of the  $^{13}\text{C} - \alpha$  relative energy is performed using only three kinematic variables, namely deuteron kinetic energy, angle of emission, and  $^{16}\text{O}$  kinetic energy, if we neglect the  $^{16}\text{O}$  angle of emission, the different target thickness produces a negligible difference in energy resolution. Using Equation (18), the uncertainty on  $E_{c.m.}$  can be calculated by propagating the above-mentioned sources; a theoretical energy resolution of  $45$  keV ( $48$  keV) was computed in the case of the  $53 \mu\text{g cm}^{-2}$  ( $107 \mu\text{g cm}^{-2}$ ) target, which is in perfect agreement with the experimental values. Moreover, the good agreement makes it clear that no systematic errors connected to the target, such as outgoing particle energy reconstruction or background subtraction, makes a significant contribution to the total experimental error.

Since the two datasets in Figure 10 are fully consistent with each other, a weighed sum of the two was calculated, which is shown in Figure 11 (upper panel). The THM cross section  $d^3\sigma / (dE_{c.m.} d\Omega_{c.m.} d\Omega_d)$  is given in arbitrary units as solid circles. It clearly shows the presence of several resonances in the  $^{13}\text{C} - \alpha$  relative energy spectrum, centered at  $\sim -3$  keV,  $\sim 810$  keV, and  $\sim 1.02$  keV. These peaks corresponds to  $^{17}\text{O}$  states at

6.356 MeV ( $J^\pi = 1/2^+$ ), 7.165 MeV ( $J^\pi = 5/2^-$ ), 7.248 MeV ( $J^\pi = 3/2^+$ ), 7.378 MeV ( $J^\pi = 5/2^+$ ), and 7.381 MeV ( $J^\pi = 5/2^-$ ), as marked by arrows in the upper panel of Figure 11 (resonance energies are taken from Tilley et al. 1993; Heil et al. 2008). As mentioned in La Cognata et al. (2012), using the approach already applied by La Cognata et al. (2011), we performed a preliminary analysis based on Equation (14), introducing the resonance parameters in Heil et al. (2008). The reason is that resonances contribute with different strengths to the THM cross section and to the direct, OES one, so a preliminary evaluation of their strengths is necessary to correctly identify the  $^{17}\text{O}$  states populated in this measurement. It turns out that the 7.248 MeV and the 7.381 MeV states make minor contribution ( $\sim 3\%$ ) to the THM yield, so the three observed resonances in Figure 11 have to be attributed to the  $^{17}\text{O}$  levels at 6.356 MeV, 7.165 MeV, and 7.378 MeV. The last two peaks look broader in the THM spectra (showing a full width at half-maximum (FWHM) of about 100 keV than what is listed in the  $^{17}\text{O}$  level parameter compilations (Tilley et al. 1993; Heil et al. 2008, who reported a FWHM of the order of 1 keV), owing to the  $^{13}\text{C} - \alpha$  relative energy resolution attained in the present experiment, as discussed before.

A fit of the THM cross section  $d^3\sigma/dE_{c.m.}d\Omega_{c.m.}d\Omega_d$  has been performed to disentangle the different peaks correlated to the  $^{17}\text{O}$  states we have identified. The sum of three Gaussian curves to account for the 6.356 MeV, 7.165 MeV, and 7.378 MeV levels, and a straight line to account for the uncorrelated background, has been adopted as a fitting function, where the position of the resonances has been fixed to the theoretical values. A fit of the THM data is necessary for two reasons, namely, for an angular distribution integration over  $\Omega_{c.m.}$ , the neutron emission angle in the center-of-mass system of the sub-reaction  $^{13}\text{C}(\alpha, n)^{16}\text{O}$ , and for background elimination. Its existence is apparent from the relative energy spectra in Figure 8, where a structureless continuum shows up in the inter-resonance regions. The contribution of the background is well described by a horizontal line, represented by a green line in Figure 11. A light blue, brown, and blue line are used instead to highlight the resonances at  $-3$  keV, 806 keV, and 1019 keV, respectively. The sum of these functions is shown as a red line in the lower panel of Figure 11, superimposed on the background subtracted THM cross section (solid circles). Good agreement within the uncertainties makes us confident of an accurate background subtraction procedure; moreover, it lead us to the conclusion that background removal does not introduce further errors to the THM cross section.

### 5.1. From the Experimental $^{13}\text{C}(^6\text{Li}, n^{16}\text{O})d$ Cross Section to the Angle Integrated Cross Section $d^2\sigma/dE_{c.m.}d\Omega_d$

The experimental differential cross section of the  $^{13}\text{C}(\alpha, n)^{16}\text{O}$  virtual reaction covers only a small angular range, from  $110^\circ$  to  $140^\circ$ , so angular integration with respect to  $\theta_{c.m.}$  was performed calculating the theoretical angular distributions. The coverage of a narrow range has to be ascribed to the analysis of a single coincidence couple, spanning a limited phase space region. In the center-of-mass of the system of the sub-reaction,  $\theta_{c.m.}$  is the angle between the momentum of any of the two fragments ( $n$  or  $^{16}\text{O}$ ) and the virtual beam direction. Therefore, it is defined as

$$\theta_{c.m.} = \arccos(\hat{\mathbf{k}}_{\alpha^{13}\text{C}} \cdot \hat{\mathbf{k}}_{n^{16}\text{O}}), \quad (19)$$

where the relative momenta  $\hat{\mathbf{k}}_{ij} = \mathbf{k}_{ij}/k_{ij}$  between particles  $i, j$  are invariant under Galilean transformations, i.e., they

remain the same in any coordinate system. Hence, they can be calculated using the momenta in the laboratory system, where the momentum of the transferred  $\alpha$  is equal and opposite to that of the deuteron in  $^6\text{Li}$  center of mass, in the QF kinematics (Jain et al. 1970; Spitaleri et al. 2004; La Cognata et al. 2007, 2010a).

The general expression for the angular distribution of the fragments for the resonance reaction has been obtained by Blatt & Biedenharn (1952). In the case of an isolated resonance with only one value of  $l_i$ ,  $l_f$ ,  $S_i$ , and  $S_f$  contributing (orbital angular momenta and channel spins for the initial  $i$  and final  $f$  channels), it takes the form:

$$\begin{aligned} \frac{d\sigma}{d\Omega}(\theta_{c.m.}) &= K (-1)^{S_f - S_i} \sum_L (\hat{l}_i)(\hat{l}_f)(\hat{J}_F)^2 (-1)^L \begin{pmatrix} l_i & J_F & S_i \\ J_F & l_i & L \end{pmatrix} \\ &\times \langle l_i m_{l_i} l_i m_{l_i} | L M_L \rangle \begin{pmatrix} l_f & J_F & S_f \\ J_F & l_f & L \end{pmatrix} \\ &\times \langle l_f m_{l_f} l_f m_{l_f} | L M_L \rangle P_L(\cos \theta_{c.m.}). \quad (20) \end{aligned}$$

In this equation,  $\begin{pmatrix} l_i & J_F & S_i \\ J_F & l_i & L \end{pmatrix}$  and  $\begin{pmatrix} l_f & J_F & S_f \\ J_F & l_f & L \end{pmatrix}$  are Wigner 6j-symbols (Messiah 1962a) and  $\langle l_i m_{l_i} l_i m_{l_i} | L M_L \rangle$  and  $\langle l_f m_{l_f} l_f m_{l_f} | L M_L \rangle$  are Clebsch-Gordan coefficients (Messiah 1962b).  $K$  is a normalization constant, which in general is a function of the center-of-mass energy  $E_{c.m.}$ , reflecting the HOES nature of the differential cross section when Equation (20) is used for the HOES angular distributions.

Using  $d\sigma/d\Omega(\theta_{c.m.})$  from Equation (20), the following correction factors have been computed:

$$\Xi_i = \frac{\int_{\theta_{c.m.}^{\min}}^{\theta_{c.m.}^{\max}} \frac{d\sigma}{d\Omega}(\theta_{c.m.}) d\theta_{c.m.}}{\int_0^\pi \frac{d\sigma}{d\Omega}(\theta_{c.m.}) d\theta_{c.m.}}, \quad (21)$$

where the index  $i$  refers to the  $i$ th resonance.  $\Xi_i$  is the ratio of the theoretical differential cross section integrated over the  $(\theta_{c.m.}^{\min}, \theta_{c.m.}^{\max}) = (110^\circ, 140^\circ)$  angular range explored in the THM experiment by the PSD 2 and 5 coincidence to the total cross section. Clearly,  $\Xi_i$  does not depend on the energy as the  $K$  factors cancel out and so the HOES nature of the measured cross section has no influence on the angular distribution integration procedure (La Cognata et al. 2010a). Assuming that the experimental angular distributions are well reproduced by Equation (20), a hypothesis that will be examined later on and is well satisfied in previous investigations (La Cognata et al. 2010c, 2010a),  $\Xi_i$  can be regarded as the center-of-mass geometric detection efficiency. Then, each resonance contribution to the THM cross section, disentangled as described in the previous section, has been divided by these factors to determine the angular integrated cross section  $d^2\sigma/dE_{c.m.}d\Omega_d$ . The resonance deconvolution procedure introduces a negligible uncertainty to the overall error budget as little overlap between peaks is present.

The resulting  $d^2\sigma/dE_{c.m.}d\Omega_d$  cross section is displayed in arbitrary units as solid symbols in Figure 12. The error budget affecting the experimental data comprises statistical, background subtraction, and angular integration uncertainties, owing to the resonance separation procedure (vertical error bars). As before, the horizontal error bars delimit the energy integration bins, smaller than the energy resolution. In comparison with previous preliminary results in La Cognata et al. (2012), the experimental uncertainty is  $\sim 30\%$  lower over the entire energy range, on average, thanks to a reduction in the statistical error. In the high-energy region, above 600 keV, the average reduction of the total error is  $\sim 50\%$ , making the present work a significant improvement on previously published results (La Cognata et al. 2012).

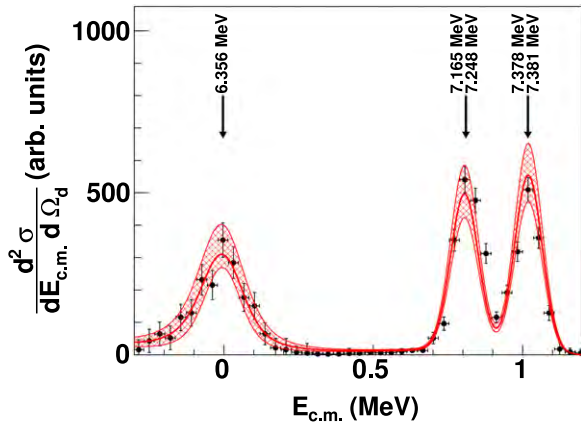


**Figure 12.** HOES  $R$ -matrix fit of THM data (Figure 11), integrated over the entire  $n$  emission angle in the  $^{13}\text{C}(\alpha, n)^{16}\text{O}$  center-of-mass system,  $\theta_{\text{c.m.}}$ . In the fit, the parameters of the resonances above 500 keV were kept fixed at the ones in Heil et al. (2008). The middle, top, and bottom red lines are used for the best fit and the upper and lower limits, respectively, set by the experimental uncertainties (statistical, background subtraction, and normalization).

(A color version of this figure is available in the online journal.)

## 6. DETERMINATION OF THE REDUCED $\gamma$ -WIDTHS FROM THE $^{13}\text{C}(\alpha, n)^{16}\text{O}$ QF CROSS SECTION

The assessment of the  $d^2\sigma/dE_{\text{c.m.}}d\Omega_d$  cross section is the starting point of the THM application. In order to link it to the OES astrophysical factor of the  $^{13}\text{C}(\alpha, n)^{16}\text{O}$  reaction, it is still mandatory to validate the THM approach in the present case and work out a normalization procedure, since the THM does not provide for absolute values in its current formulation. To these purposes, we focus on the region above 500 keV, where both direct (Davids 1968; Bair & Haas 1973; Kellogg et al. 1989; Brune et al. 1993; Drotleff et al. 1993; Harissopulos et al. 2005; Heil et al. 2008) and THM data are available, the influence of the  $-3$  keV resonance (whose evaluation is the main goal of the present work) is small, and the effect of electron screening is negligible. In particular, we compare the THM data with the  $R$ -matrix fit reported by Heil et al. (2008), as direct  $^{13}\text{C}(\alpha, n)^{16}\text{O}$  data show a broad dispersion in absolute values; the fit performed by Heil et al. (2008) combines a very large set of data, including not only the  $^{13}\text{C}(\alpha, n)^{16}\text{O}$  cross section but those of all the possible open channels, drastically reducing the systematic errors possibly affecting some experimental cross sections.

As discussed in the theoretical section, the THM data are well described by a modified  $R$ -matrix function, where the entrance channel partial width has to be replaced by a suitable function (compare Equation (14)) to take into account the virtual nature of the transferred  $\alpha$ -particle. However, Equation (14) demonstrates that the same reduced widths appear in the modified and standard  $R$ -matrix equations, therefore the ones deduced from the fitting of direct data can be inserted in Equation (14) to reproduce the THM cross section. Equation (14) has to be slightly modified, in the same way as the standard  $R$ -matrix (Lane & Thomas 1958), to comprise the interference between the 5.868 MeV and the 7.202 MeV  $3/2^+$  states (Tilley et al. 1993; Heil et al. 2008). General equations are discussed in detail in Mukhamedzhanov (2011). Here, we underscore that the reduced  $\gamma$ -widths have been determined to reproduce the partial widths given in Heil et al. (2008). The channel radii have been fixed to the ones in Heil et al. (2008) as well ( $R_{\alpha^{13}\text{C}} = 5.2$  fm and  $R_{n^{16}\text{O}} = 4.0$  fm). Such reduced  $\gamma$ -widths were used to

calculate a HOES  $R$ -matrix function to be superimposed on the THM data, including all the  $^{17}\text{O}$  levels contributing directly and through their interference to the  $-0.3$ – $1.2$  MeV energy window. The resulting HOES astrophysical factor was folded with a Gaussian with  $\sigma = 46$  keV to take into consideration energy resolution, affecting the  $E_{\text{c.m.}}$  variable, as discussed earlier in this work.

Therefore, the normalization constant NF in Equation (14) is the only free parameter necessary to match the HOES  $R$ -matrix calculation with the THM data. Even though the value assumed by the NF parameter is not important, as the  $d^2\sigma/dE_{\text{c.m.}}d\Omega_d$  cross section is expressed in arbitrary units, it allows us to estimate the height of the sub-threshold resonance relative to those of the well known resonances at energies larger than 500 keV. Since it is the same over the entire energy range, the strength of the sub threshold resonance is normalized to those of the measured resonances at 7.165 MeV, 7.248 MeV, 7.378 MeV, and 7.381 MeV. Figure 12 demonstrates that good agreement is found between the THM  $d^2\sigma/dE_{\text{c.m.}}d\Omega_d$  cross section and the calculated one above 500 keV ( $\chi^2 = 0.4$ ); to account for normalization error, a band is specified in Figure 12, displaying the upper and lower values of the scaling factor allowed for by the experimental uncertainties. Such a normalization error,  $\sim 15\%$ , will be propagated to the resonance parameters of the sub threshold peak at  $-3$  keV. The normalization error is of the same order as the one reported in our previous work (La Cognata et al. 2012). It is important to note that it is much larger than the uncertainty affecting the  $R$ -matrix fit of Heil et al. (2008), which can be estimated to be  $\sim 5\%$  at these energies from Figure 18.

The agreement is crucial as it serves as a validity test of our approach in the same way as the determination of the  $\alpha - d$  momentum distribution and the comparison with the theoretical ones. Again, to cross check our approach against the effect of distortions, the FRESCO code (Thompson 1988) has been used to calculate the ratio of the peak values of the resonances at 810 keV and 1.02 MeV in the DWBA framework. As discussed in Mukhamedzhanov (2011) and La Cognata et al. (2010a), Equation (14) can be generalized to the DWBA case, introducing the DWBA transfer cross section for the  $^{13}\text{C}(\alpha, d)^{17}\text{O}^*$  process. In the calculation, the same optical potential parameters used in Johnson et al. (2006) have been adopted; the involved nuclei are the same and the center-of-mass energies are similar. Since both 7.165 MeV and 7.378 MeV  $^{17}\text{O}$  states have narrow widths (Tilley et al. 1993), energy resolution is affecting them in a similar way, thus the comparison between the peak values is accurate; the main source of uncertainty is connected to the calculation of transfer to unbound states. The DWBA calculations reproduce the experimental results to within 9%, within the normalization error, corroborating the present results by means of a more accurate approximation. Eventual systematic errors are bound to be smaller than 9%.

Below  $E_{\text{c.m.}} = 500$  keV, the THM data clearly display the presence of a resonance located at  $-3$  keV, corresponding to the 6.356 MeV  $^{17}\text{O}$  level. For the first time, such a resonance has been observed in the  $^{13}\text{C}(\alpha, n)^{16}\text{O}$  reaction. Obviously, no direct observation is possible as it lays at negative  $\alpha - ^{13}\text{C}$  relative energies; conversely, the THM allows us to explore low and even negative energies as the  $^6\text{Li} = \alpha + d$  binding energy and the  $\alpha - d$  relative motion associated energy compensate for the beam energy. Moreover, no Coulomb hampering of the cross section nor electron screening spoil the low-energy trend in the THM approach. Therefore, as already shown in our preliminary

analysis in La Cognata et al. (2012), the  $^{13}\text{C}(\alpha, n)^{16}\text{O}$   $S$ -factor can be inferred with unprecedented accuracy.

Having fixed the NF of the HOES  $R$ -matrix calculation, we can extract the resonance parameters of the  $-3$  keV, scaled to the partial widths of the higher energy resonances from Heil et al. (2008) using the HOES  $R$ -matrix formula to fit the THM cross section at  $E_{\text{c.m.}} < 500$  keV. Only two fitting parameters, namely  $\gamma_n$  and  $\gamma_\alpha$ , have to be deduced from the experimental data. We underscore that THM is the only approach that yields both  $\Gamma_n$  and  $\Gamma_\alpha$  from the same dataset, so we do not need to take  $\Gamma_n$  from the literature, as in previous works (Johnson et al. 2006; Pellegriti et al. 2008; Guo et al. 2012, for instance) did, nor do we have to extrapolate the trend of the  $^{13}\text{C}(\alpha, n)^{16}\text{O}$   $S$ -factor. These procedures may possibly incur systematic uncertainties due to electron screening or neutron measurements (as in Harissopoulos et al. (2005), as discussed in Heil et al. (2008)). The best-fit curve, together with the upper and lower limits allowed by statistical and systematic uncertainties, are presented in Figure 12; an overall  $\tilde{\chi}^2 = 2.2$  is obtained. The effect of energy resolution, which could introduce systematic effects into the THM result, has been fully taken into account as in La Cognata et al. (2009). However, it is not significantly influencing the fit of the  $-3$  keV peak as this resonance is comparatively broad.

From the reduced widths, the observable partial width  $\Gamma_n^{1/2+}$  of the  $-3$  keV resonance has been calculated, yielding  $107 \pm 5_{\text{stat}}^{+9}_{-5} \text{ norm keV}$ , larger than the  $\Gamma_n^{1/2+} = 83_{-12}^{+9} \text{ keV}$  value obtained in our preliminary analysis (La Cognata et al. 2012) and slightly smaller than the value usually adopted in the literature,  $124 \pm 12 \text{ keV}$  Tilley et al. (1993) and the one reported in Heil et al. (2008):  $158 \text{ keV}$ . The THM approach allowed us to extract the Coulomb-modified ANC  $\tilde{C}_{\alpha^{13}\text{C}}^{17\text{O}(1/2^+)}$  of the  $-3$  keV resonance as well, from the HOES  $R$ -matrix fitting of the THM data. Again, this is the first time that the THM has been used to extract the ANC of a sub-threshold resonance. In detail, following the discussion in Mukhamedzhanov & Tribble (1999) and La Cognata et al. (2012) and the theoretical section of this work, we obtained  $(\tilde{C}_{\alpha^{13}\text{C}}^{17\text{O}(1/2^+)})^2 = 7.7 \pm 0.3_{\text{stat}}^{+1.6}_{-1.5} \text{ norm fm}^{-1}$  in agreement, within the uncertainties, with our preliminary value  $6.7_{-0.6}^{+0.9} \text{ fm}^{-1}$ . Table 2 shows the ANCs for previous measurements and, where these quantities were not available, the spectroscopic  $S_\alpha$  factors for the  $6.356 \text{ keV } ^{17}\text{O}$  level. This comparison indicates that our result is consistent with the ANC deduced from the spectroscopic factor measurement by Pellegriti et al. (2008) and probably with the result of Guo et al. (2012), once the increase in  $S_\alpha$  for the increasing beam energy observed by Pellegriti et al. (2008) is accounted for. We can also infer that our result is in agreement with the analysis of Keeley et al. (2003), although they do not cite either the ANC value nor the experimental uncertainty, as the spectroscopic factor they obtained is within the window reported by Guo et al. (2012). Conversely, the  $(\tilde{C}_{\alpha^{13}\text{C}}^{17\text{O}(1/2^+)})^2$  value of the present work is significantly larger than the ANC in Johnson et al. (2006) and Kubono et al. (2003) (compare Table 2), calling for a more exhaustive investigation of the  $\alpha$ -transfer reaction used to populate the  $6.356 \text{ keV } ^{17}\text{O}$  level, as systematic errors might be present.

Figure 13 shows the comparison of the THM  $S(E)$ -factor of the  $^{13}\text{C}(\alpha, n)^{16}\text{O}$  reaction with direct data from Davids (1968), Bair & Haas (1973), Kellogg et al. (1989), Brune et al. (1993), Drotleff et al. (1993), Harissopoulos et al. (2005) and Heil et al. (2008). The former was obtained by introducing the reduced widths of the  $-3$  keV resonance into a standard  $R$ -matrix code

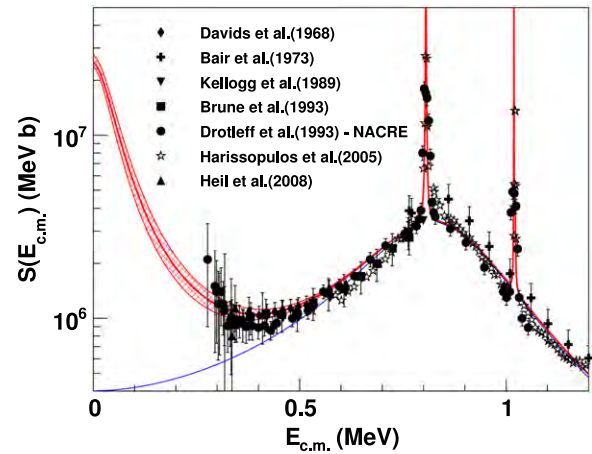


**Figure 13.**  $S(E)$ -factor (red middle line), obtained from the  $R$ -matrix using the THM resonance parameters below  $E_{\text{c.m.}} = 500$  keV and the Heil et al. (2008) parameters above. The upper and lower red lines mark the range allowed by experimental errors affecting the THM data in Figure 12 and by the normalization uncertainty. The  $R$ -matrix  $S(E)$ -factor not including the sub-threshold resonance at  $-3$  keV is indicated by the blue line. Black symbols are direct data, normalized as in Heil et al. (2008). Different marks are used for each dataset as specified in the inset. In particular, the data from Drotleff et al. (1993) were taken as references in the NACRE compilation (Angulo et al. 1999).

(A color version of this figure is available in the online journal.)

(Lane & Thomas 1958), including all the resonances inside the  $0$ – $1.2$  MeV energy region and those influencing this interval through their tails or interference with other resonances. This is possible as the same reduced widths appear in the OES  $S(E)$ -factor and in the modified  $R$ -matrix approach; the only difference is the absence of any Coulomb or centrifugal penetration factor in the entrance channel neither of the electron screening effect (see Equation (14)). The result is given in Figure 13 as a red band; the middle line is the best fit curve and the upper and lower red lines delineate the recommended range allowed by the statistical, normalization, and data reduction uncertainties. Only the uncertainty due to the  $-3$  keV resonance is displayed; the error due to the accuracy of the  $R$ -matrix fit of Heil et al. (2008), which is used for normalization, is smaller than 5%. For comparison, the  $S$ -factor omitting the contribution of the  $6.356 \text{ MeV } ^{17}\text{O}$  level is also shown in this figure as a blue line. The black points represent the available direct  $^{13}\text{C}(\alpha, n)^{16}\text{O}$  data from Heil et al. (2008) and references therein, namely, scaled to match the high-precision data reported in this work. In particular, the lowest energy data are from Drotleff et al. (1993), who corrected the  $S$ -factor for electron screening. A very good agreement is found between the THM  $S(E)$ -factor and experimental data, as should be expected since no electron screening alters the low-energy trend.

## 7. COMPARISON WITH PREVIOUS STUDIES

Figure 14 shows the juxtaposition of the THM  $S(E)$ -factor of the  $^{13}\text{C}(\alpha, n)^{16}\text{O}$  reaction and the direct data, as in Figure 13, but restricted to the  $0.1$ – $0.6$  MeV range, where the contribution of the  $6.356 \text{ MeV } ^{17}\text{O}$  state is larger. In particular, a linear scale is used for ease of comparison. Direct data are taken from Davids (1968), Bair & Haas (1973), Kellogg et al. (1989), Brune et al. (1993), Drotleff et al. (1993), Harissopoulos et al. (2005) and Heil et al. (2008) and the same symbols as in Figure 13 are employed to differentiate the datasets. In the upper panel, direct data are shown as they were reported in the original works and different colors are used to emphasize

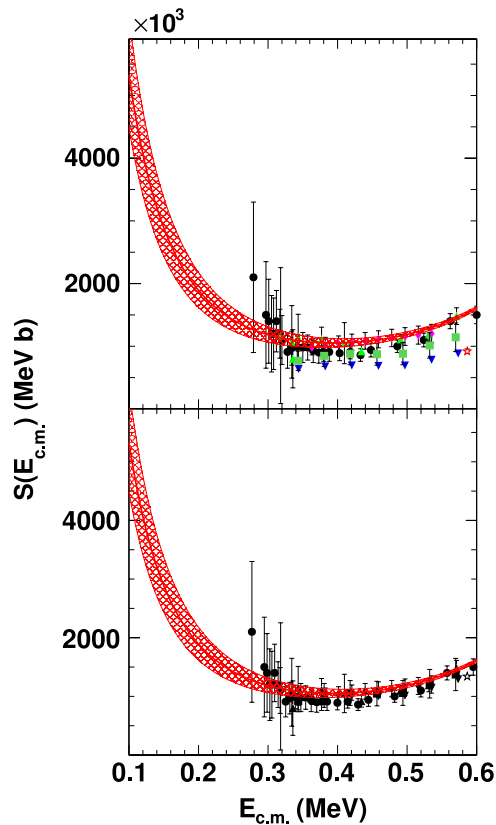


**Figure 14.** Comparison of the THM  $S$ -factor (red band as in Figure 13) with direct data. We zoom in on the low-energy region for ease of comparison. In the upper panel, direct data (Davids 1968; Bair & Haas 1973; Kellogg et al. 1989; Brune et al. 1993; Drotleff et al. 1993; Harissopoulos et al. 2005; Heil et al. 2008) are taken from the original works (no scaling). The symbols used to distinguish the different datasets are the same as in Figure 13, although with different colors. The change in color is used to highlight those datasets with their original normalization. In the lower panel, on the other hand, the THM  $S$ -factor is superimposed on the direct data scaled as recommended by Heil et al. (2008).

(A color version of this figure is available in the online journal.)

the renormalized datasets. In contrast, in the lower panel, the direct data are rescaled following the prescription in Heil et al. (2008). Figure 14 shows that good agreement is found between the THM  $R$ -matrix and the direct data once these have been corrected according to the considerations in Heil et al. (2008); this is what should be expected above 500 keV as we used the Heil et al. (2008)  $R$ -matrix curve for normalization. The agreement between the scaled data and the THM  $S(E)$ -factor below 500 keV corroborates the remarks by Heil et al. (2008) about systematic errors possibly affecting some astrophysical factors in the literature.

In Figure 15, the THM  $S(E)$ -factor is compared with some of the available extrapolations of the direct  $^{13}\text{C}(\alpha, n)^{16}\text{O}$  astrophysical factor. Only the low-energy region of interest for astrophysics is displayed. In the upper panel, the THM  $S(E)$ -factor (red hatched region) is contrasted with extrapolations based on direct data. In particular, the blue band highlights the astrophysical factor range allowed by the uncertainties, as deduced by Heil et al. (2008) using a very broad pool of experimental data. A good agreement is found within the experimental errors, which are notably reduced in the THM  $S$ -factor with respect to the Heil et al. (2008) extrapolation. Thanks to the direct observation of the  $-3$  keV resonance in the THM approach, the experimental errors have decreased from about a factor of two at 100 keV to

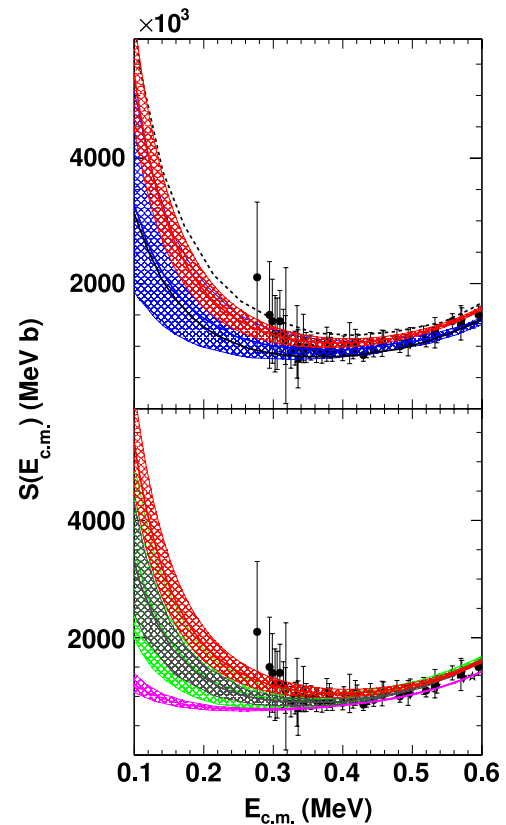


**Figure 15.** Upper panel: comparison of some commonly adopted  $R$ -matrix extrapolations with the  $R$ -matrix function obtained from the experimental THM resonance parameters of the 6.356 MeV  $^{17}\text{O}$  state. The THM result (Figure 12) is shown as a red band. A blue band is used to mark the  $R$ -matrix fit in Heil et al. (2008), while the extrapolations of Drotleff et al. (1993) and Hale (1997) are shown as a solid black line and a short-dashed black line, respectively. Lower panel: comparison of the THM-based  $R$ -matrix formula (red band) with those derived from previous indirect measurements. Purple, green, and gray hatched bands denote Johnson et al. (2006), Pellegriti et al. (2008), and Guo et al. (2012) calculations, respectively, based on their measurement of the 6.356 MeV state ANC or spectroscopic factor.

(A color version of this figure is available in the online journal.)

$\sim 20\%$ . The recommended THM  $S$ -factor at  $E_{c.m.} = 100$  keV is  $5.3 \pm 0.9 \times 10^6$  MeVb, about 40% larger than the value provided by Heil et al. (2008) (see Table 1). In the same panel, two extrapolations widely adopted in most astrophysical calculations are also presented, the Breit-Wigner fit of Drotleff et al. (1993), shown as a black solid line, and the  $R$ -matrix in Hale (1997; in agreement with the  $S$ -factor recommended by the NACRE compilation (Angulo et al. 1999)), identified by a black short-dashed line. Even though no errors are cited for these calculations, from Figure 15 (upper panel) it turns out that the THM result lies in between the two, approaching the Hale (1997) one at the lowest energies.

In Figure 15 (lower panel), the THM astrophysical factor is superimposed on the  $R$ -matrix functions obtained using the ANC or the spectroscopic factor of the 6.356 MeV  $^{17}\text{O}$  state with respect to the  $^{13}\text{C} - \alpha$  channel, as deduced through alternative indirect approaches. In detail, the THM  $S(E)$  overlaps with the one from Pellegriti et al. (2008), where the ANC and the spectroscopic factor for the  $^{17}\text{O} \rightarrow \alpha + ^{13}\text{C}$  configuration is deduced from the  $\alpha$ -transfer off  $^7\text{Li}$ , and with the one from Guo et al. (2012) once all the sources of uncertainties are taken into consideration. The THM result proves to be more accurate as no extrapolation or spectroscopic factor measurement is

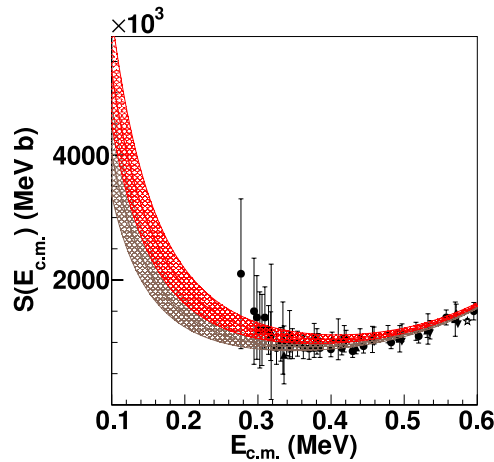


**Figure 16.**  $R$ -matrix formula of the present work (red hatched area; the same as in Figure 12) superimposed on the  $R$ -matrix calculation given in La Cognata et al. (2012), where the resonance parameters of the 6.356 MeV  $^{17}\text{O}$  state were deduced from a partial dataset (brown hatched area). The  $S$ -factor of the present work is larger than the previous  $S$ -factor owing to the larger ANC of the sub threshold resonance.

(A color version of this figure is available in the online journal.)

necessary to infer the  $^{13}\text{C}(\alpha, n)^{16}\text{O}$   $S$ -factor. In particular, the extraction of the spectroscopic factor  $S_\alpha$  might introduce significant systematic uncertainties due to ambiguities in the optical potentials. In this way, the uncertainty is reduced from  $\sim 45\%$  (Pellegriti et al. 2008) to  $\sim 20\%$  (present work). As in La Cognata et al. (2012), the Johnson et al. (2006) calculation shown as a purple band, based on the measurement of the ANC  $(\tilde{C}_{\alpha^{13}\text{C}}^{^{17}\text{O}(1/2^+)})^2$  using the sub-Coulomb  $^6\text{Li}(^{13}\text{C}, d)^{17}\text{O}$  transfer reaction, is much lower than the  $S$ -factor of the present work; it is about a factor of three smaller than the extrapolation in Heil et al. (2008) at  $\sim 100$  keV. This is connected to the comparatively small Coulomb-corrected ANC deduced in their work, probably due to some unidentified systematic error.

Our results are in fair agreement with the independent calculation of Dufour & Descouvemont (2005), who predicted  $S(100 \text{ keV}) = 5.3 \times 10^6 \text{ MeVb}$  by applying the microscopic two-cluster model (as shown in Table 1). This calculation improved previous studies (Descouvemont 1987) and, in particular, allowed one to accurately reproduce the sub threshold  $1/2^+$  resonance.

Finally, Figure 16 shows the comparison between the  $S$ -factor obtained in La Cognata et al. (2012), based on the preliminary value of  $(\tilde{C}_{\alpha^{13}\text{C}}^{^{17}\text{O}(1/2^+)})^2$  derived from a partial dataset (brown hatched region) and the  $S$ -factor deduced in the present work (red band as before). Because of the larger value of the ANC given here, the astrophysical factor undergoes a steeper increase with decreasing energy with respect to the behavior inferred in the letter (La Cognata et al. 2012), still in agreement within uncertainties. These are comparable in both works, demonstrating that statistical error, here reduced as a consequence of the larger statistics, is not the principal source of uncertainty affecting the THM measurement. This is clear when examining the error budget affecting the ANC of the 6.356 MeV resonance, as the statistical uncertainty represents only  $\sim 20\%$  of the total error. From the comparison of the preliminary  $R$ -matrix calculation and the one based on the full dataset, the better agreement of the latter with the lowest energy data from Drotleff et al. (1993) is apparent.

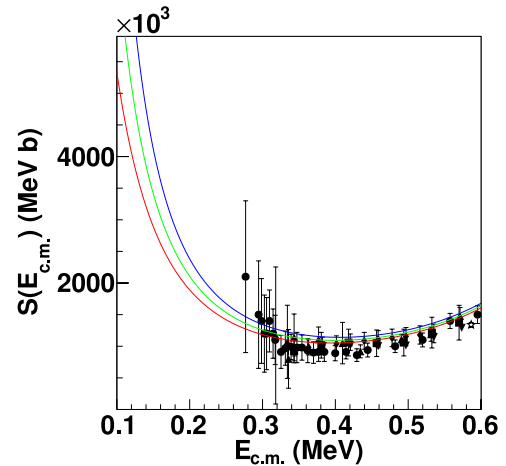


**Figure 17.** Comparison between direct data (black symbols as in the previous figures) and the low-energy, bare-nucleus THM  $S$ -factor (red line). In particular, the Drotleff et al. (1993) dataset is taken from the Angulo et al. (1999) compilation (same as in Heil et al. 2008), where no correction for the electron screening enhancement has been performed (F. Strieder 2013, private communication). A blue line is used for the screened  $S$ -factor, assuming an electron screening potential  $U_e = 2 \text{ keV}$  (Assenbaum et al. 1987), and a green line is used for the screened astrophysical factor obtained by introducing the potential  $U_e$  into the enhancement factor, calculated using the adiabatic approach (F. Strieder 2013, private communication; Bracci et al. 1990), 0.937 keV.

(A color version of this figure is available in the online journal.)

## 8. THE ELECTRON SCREENING EFFECT

As pointed out in the introductory sections, the electron screening effect plays a crucial role in the determination of the  $^{13}\text{C}(\alpha, n)^{16}\text{O}$   $S$ -factor at astrophysical energies using direct approaches. Indeed, an impinging nucleus sees no repulsive nuclear Coulomb force until it penetrates beyond the atomic radius. Therefore, at low beam energies, where the classical turning point for bare nuclei is close to the atomic radius, the projectile is subject to a less repulsive potential (Assenbaum et al. 1987; Rolfs & Rodney 1988). This results in an enhancement of the cross section relative to the value it would assume for fully ionized interacting particles, described by the enhancement factor:

$$f_{\text{enh}} = \exp \left[ \pi \eta \frac{U_e}{E_{\text{c.m.}}} \right], \quad (22)$$

where  $\eta = Z_x Z_A e^2 / \hbar v_{xA}$  is the Sommerfeld parameter for the entrance channel ( $v_{xA}$  is the  $x$ - $A$  relative velocity) and  $U_e$  is the electron screening potential, basically the energy transfer from the atomic to the nuclear degrees of freedom (Bracci et al. 1990). Atomic physics dictates an upper bound to the value of this parameter, referred to as the adiabatic limit (Bracci et al. 1990; Rolfs & Rodney 1988; Shoppa et al. 1993). In the case of collisions at low velocity, which is the most important case for astrophysical applications, the dynamical equation for electron motion can be solved in the adiabatic approximation. It means that during the collision, the electron wave function re-adjusts itself so that at any time it is an eigenfunction of the two-center Hamiltonian. Consequently,  $U_e$  equals the difference between the sum of the energies of the isolated atoms and the energy of the united atomic system (Bracci et al. 1990). In particular, in the case of the  $^{13}\text{C}(\alpha, n)^{16}\text{O}$  reaction, the adiabatic limit leads to  $U_e = 0.937 \text{ keV}$  (F. Strieder 2013, private communication).

Figure 17 shows the comparison between the screened astrophysical factor with the available direct data at low energies (black symbols), where the effect of the electron screening is

more sizable. In particular, the lowest energy data points (from Drotleff et al. 1993) are not extracted from the original work, where they have been corrected for the electron screening effect, but rather from the NACRE compilation (Angulo et al. 1999), as in Heil et al. (2008). The shielded  $S$ -factor is computed taking as the bare-nucleus  $S$ -factor the one supplied by the THM (red line, as in the previous figures), multiplied by the enhancement factor Equation (22). In detail, the screened  $S$ -factor deduced by inserting the adiabatic limit electron screening potential into  $f_{\text{enh}}$  is given as a green line while the top blue line represents a larger value  $U_e = 2$  keV, as reported by Assenbaum et al. (1987). This last value leads to an enhancement factor closer to the one estimated by Drotleff et al. (1993). Although this last value is likely to overestimate the electron screening potential (exceeding the adiabatic limit, although several measurements have demonstrated that the experimental  $U_e$  can be larger than the adiabatic limit; see for instance La Cognata et al. (2005) and references therein), experimental uncertainties affecting direct data are so large that it is not possible to attain a significant estimate of  $U_e$  from the comparison between the THM  $S$ -factor and direct data or rule out unsatisfactory models for the calculation of  $U_e$ . This result definitely calls for improved direct measurements of the low-energy astrophysical factor of the  $^{13}\text{C}(\alpha, n)^{16}\text{O}$  reaction aimed at the investigation of the electron screening effect in the case of resonance reactions. This confirms once more that the THM is an useful approach, complementary to direct measurements.

## 9. REACTION RATE FOR $^{13}\text{C}(\alpha, n)^{16}\text{O}$

The charged-particle thermonuclear reaction rate is calculated from the  $S(E)$ -factor using the following standard integral (Iliadis 2007):

$$N_A \langle \sigma v \rangle = N_A \sqrt{\frac{8}{\pi \mu (k_B T)^3}} \int_0^\infty e^{-2\pi\eta} S(E) e^{\frac{-E}{k_B T}} dE, \quad (23)$$

where  $\mu$  is the reduced mass of the projectile-target system,  $N_A$  is Avogadro's number,  $k_B$  is the Boltzmann constant,  $T$  is the temperature,  $\eta$  is the Sommerfeld parameter, and  $E$  is the energy in the center-of-mass system. The reaction is assumed to involve bare nuclei, thus it does not take into account electron screening effects. In this paper, the reaction rate  $R$  has been calculated introducing into Equation (23) the THM astrophysical factor. The resulting  $^{13}\text{C}(\alpha, n)^{16}\text{O}$  reaction rate is tabulated in Table 3 as a function of the temperature parameter  $T_9 (= T/10^9 \text{ K})$ . We report the adopted rate with the corresponding lower and upper limits expressed in units of  $\text{cm}^3 \text{ mol}^{-1} \text{ s}^{-1}$ . The fifth column contain the exponent of the power of 10 factor that is relevant to columns 2–4.

Figure 18 (upper panel) shows the reaction rates listed in Table 3. Upper and lower limits are also given, but they are barely visible because of the steep decrease of  $R$  with decreasing temperature and the fairly small errors. These add up to about 16%, slightly improving the result obtained in the previous work by La Cognata et al. (2012) and confirming the accuracy of the technique. In the lower panel, we compare the present  $^{13}\text{C}(\alpha, n)^{16}\text{O}$  reaction rate with the one reported in Heil et al. (2008) ( $R_{\text{Heil}}$ ). For ease of comparison, the quantity  $R/R_{\text{Heil}}$  is given, namely, the ratio of each reaction rate  $R$  to the one reported in Heil et al. (2008,  $R_{\text{Heil}}$ ). In this way, the strong temperature dependence is divided out and small differences became more evident. In this representation, the Heil et al. (2008) reaction

**Table 3**  
Reaction Rates of the  $^{13}\text{C}(\alpha, n)^{16}\text{O}$  Reaction

Temperature ( $T_9$ )	Reaction Rate ( $\text{cm}^3 \text{ s}^{-1} \text{ mol}^{-1}$ )			
	Adopted	Lower	Upper	Power
0.01	2.52	2.22	2.87	-47
0.02	2.78	2.38	3.22	-34
0.03	5.17	4.37	6.04	-28
0.04	4.40	3.70	5.15	-24
0.05	2.66	2.24	3.12	-21
0.06	3.47	2.93	4.05	-19
0.07	1.68	1.42	1.95	-17
0.08	4.10	3.48	4.75	-16
0.09	6.08	5.19	7.03	-15
0.10	6.20	5.32	7.13	-14
0.11	4.72	4.07	5.40	-13
0.12	2.85	2.47	3.24	-12
0.13	1.42	1.24	1.61	-11
0.14	6.07	5.33	6.85	-11
0.15	2.27	2.01	2.56	-10
0.16	7.63	6.78	8.54	-10
0.18	6.55	5.88	7.25	-9
0.20	4.21	3.82	4.62	-8
0.25	1.83	1.70	1.97	-6
0.30	3.49	3.31	3.68	-5
0.35	3.93	3.79	4.09	-4
0.40	3.16	2.99	0.00	-3
0.45	1.84	1.78	0.02	-2
0.50	8.51	8.27	0.09	-2
0.60	1.00	0.99	1.01	0
0.70	6.57	6.53	6.62	0
0.80	2.84	28.21	2.82	1
0.90	9.05	90.12	9.01	1
1.00	2.32	2.31	2.33	2

**Notes.** The recommended value and lower and upper limits were computed between  $T_9 = 0.01$  and 1 covering the interesting astrophysical region. In the last column, the exponent of the power of 10 multiplying Columns 2, 3, and 4 is given.

rate is displayed as a horizontal line, equal to 1 over the entire temperature range. The ratio of the THM rate to the one obtained by Heil et al. (2008) is given by the red lines (the recommended value and the lower and upper limits are used to obtain the middle, lower, and upper red lines, respectively); the red band thus delimits the interval allowed by the uncertainties on the THM rate. Other rates available in the literature (Drotleff et al. 1993; Angulo et al. 1999; La Cognata et al. 2012) and widely used in stellar evolutionary and nucleosynthesis codes are also shown in Figure 18(b), divided by the Heil et al. (2008) rate. In particular, the black hatched area indicates the NACRE rate divided by the Heil et al. (2008) one; the recommended value is used to calculate the middle black line (Angulo et al. 1999). The solid black line highlights the ratio of the Drotleff et al. (1993) rate to  $R_{\text{Heil}}$  and, finally, the brown line is obtained from the ratio of the rate based on the preliminary results of La Cognata et al. (2012) to  $R_{\text{Heil}}$ . To improve the clarity of the plot, we used the same colors and styles from Figures 15 and 16.

At the astrophysically relevant temperatures  $T = 0.08\text{--}0.1 \times 10^9 \text{ K}$ , the rate from the present work agrees, within errors, with the NACRE (Angulo et al. 1999) compilation and there is only a small difference ( $\sim 15\%$ ) between the two adopted values. The present reaction rate is also 35% higher than the one suggested in La Cognata et al. (2012) and obtained with the same approach, but using a partial dataset. A very similar discussion is also valid

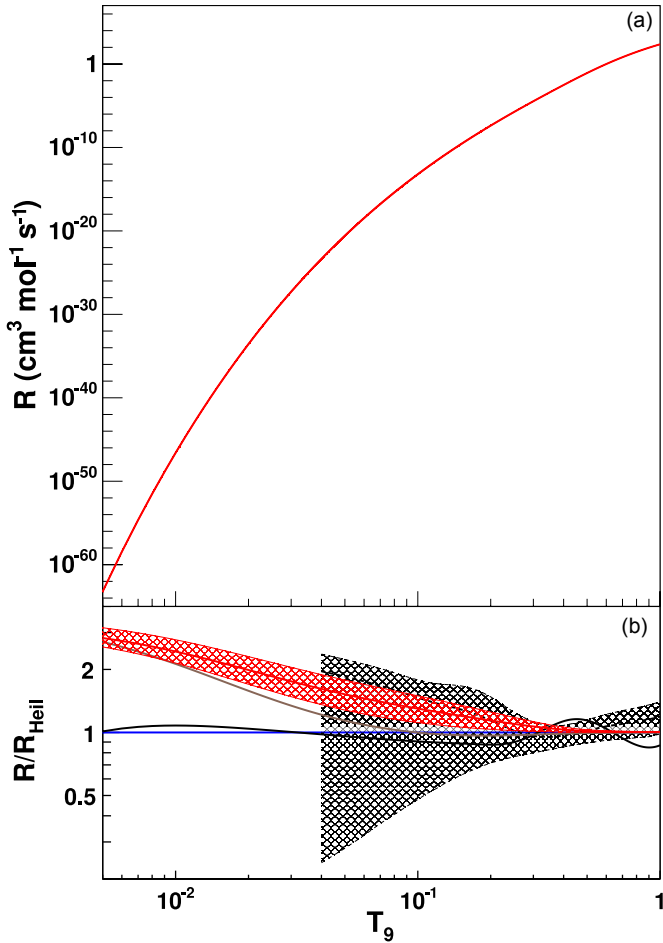


**Figure 18.** (a) Reaction rates for the  $^{13}\text{C}(\alpha, n)^{16}\text{O}$  reaction calculated from the  $S(E)$ -factor in Figures 13 and 14. The upper and lower limits are indistinguishable because of the broad rate range. (b) Ratios of several reaction rates available in the literature compared with the one of Heil et al. (2008; blue line), considered to be a reference value (equal to 1 in this representation). The red line represents the rate of the present work, while the brown line refers to the results of La Cognata et al. (2012). A solid black curve is used for the Drotleff et al. (1993) rate, while the NACRE one (Angulo et al. 1999) is illustrated by the dotted black line. The range allowed for by the uncertainties is shown by the black hatched area.

(A color version of this figure is available in the online journal.)

for  $R_{\text{Heil}}$ , because it is only 1% smaller than the reaction rate derived by the first application of the THM (La Cognata et al. 2012). A larger discrepancy ( $\sim 45\%$ ) is found with respect to the Drotleff et al. (1993) rate due to the fact that this study used only a theoretical extrapolation for energies lower than 270 keV.

At very low temperatures (about  $10^7$  K), beyond the range so far considered to be of astrophysical interest for the  $s$ -process, while the THM measurements lead to very similar reaction rates, a difference up to a factor of two is found between our rates and the two by Heil et al. (2008) and Drotleff et al. (1993). In this context, it is interesting to examine the effect of the new rate for the  $^{13}\text{C}(\alpha, n)^{16}\text{O}$  reaction concerning the  $s$ -process nucleosynthesis.

Based on the reaction rate of the present work, we recommend an analytical expression assuming the same formulas employed in the REACLIB library (Thielemann et al. 1987). This expression is valid over the whole temperature range of astrophysical interest,  $0.01 \leq T_9 \leq 1$ , and reproduces the tabulated values

**Table 4**  
Table of Coefficients of the Analytical Approximation of the  $^{13}\text{C}(\alpha, n)^{16}\text{O}$  Reaction Rate using Equations (24) and (25)

$a_{ij}$	$f_1$	$f_2$	$f_3$
$a_{i1}$	$0.605351 \times 10^{+2}$	$-0.119396 \times 10^{+2}$	$0.224751 \times 10^{+2}$
$a_{i2}$	$-0.101843 \times 10^{-1}$	$-0.119279 \times 10^{+1}$	$-0.961092 \times 10^{+1}$
$a_{i3}$	$-0.296081 \times 10^{+2}$	$-0.468285 \times 10^{+0}$	$-0.653712 \times 10^{+1}$
$a_{i4}$	$-0.387799 \times 10^{+2}$	$0.249635 \times 10^{+2}$	$-0.627747 \times 10^{+1}$
$a_{i5}$	$0.147871 \times 10^{+2}$	$0.499220 \times 10^{+0}$	$0.183825 \times 10^{+1}$
$a_{i6}$	$-0.282106 \times 10^{+1}$	$-0.717315 \times 10^{+1}$	$0.226094 \times 10^{+1}$
$a_{i7}$	$0.459746 \times 10^{+1}$	$0.836497 \times 10^{+1}$	$-0.598376 \times 10^{+1}$

within an accuracy of about 1.5%. The formula is

$$N_A \langle \sigma v \rangle = \sum_{i=1}^3 f_i, \quad (24)$$

where

$$f_i = \exp[a_{i1} + a_{i2}T_9^{-1} + a_{i3}T_9^{-1/3} + a_{i4}T_9^{1/3} + a_{i5}T_9 + a_{i6}T_9^{5/3} + a_{i7}\ln(T_9)]. \quad (25)$$

The parameters  $a_{ij}$  (with  $1 \leq i \leq 3$  and  $1 \leq j \leq 7$ ) are given in Table 4 for our recommended  $^{13}\text{C}(\alpha, n)^{16}\text{O}$  reaction rate. The fit was performed using the reaction rate parameterizer belonging to the NUCASTRODATA toolkit.<sup>7</sup>

## 10. ASTROPHYSICAL IMPLICATIONS AND CONCLUDING REMARKS

In previous sections we extensively discussed recent measurements of the astrophysical  $S(E)$ -factor for the  $^{13}\text{C}(\alpha, n)^{16}\text{O}$  reaction obtained with the indirect technique of the THM. The experiment explored very low energies (below 270 keV and also negative values), allowing us to investigate, with no need for theoretical extrapolation, the sub threshold resonance of  $^{17}\text{O}$  at  $-3$  keV in the center-of-mass system that strongly influences the astrophysical factor inside the Gamow peak region in stellar interiors. The ANC  $\tilde{C}_{\alpha^{13}\text{C}}^{17\text{O}(1/2^+)}$  of the same resonance was derived from the THM data in order to discriminate among the inconsistent results of previous investigations. Then, the reaction rate was calculated with standard equations and compared with those most used in stellar evolutionary and nucleosynthesis codes. Since the present rate is smaller than the NACRE one (Angulo et al. 1999) and larger than the Heil et al. (2008) and Drotleff et al. (1993) rates, it is interesting to know the astrophysical consequences of the new measurement concerning  $s$ -process nucleosynthesis.

The  $^{13}\text{C}(\alpha, n)^{16}\text{O}$  reaction is the main neutron source for low-mass AGB stars during the quiet radiative phase between two subsequent thermal instabilities. We used a post-process code (NEWTON) developed by the astrophysics group of the University of Perugia for the production of heavy elements via slow neutron captures for stars less massive than  $\sim 3 M_{\odot}$ . In the present paper, in particular, we consider a star of  $1.5 M_{\odot}$  and metallicity  $Z = 0.01$ , slightly less than solar, because it is one of the most commonly used stellar models (Gallino et al. 1998; Busso et al. 1999). Following the FRANEC evolutionary code (Straniero et al. 2003), the above star performs 10 thermal pulses and 10 third dredge-up episodes to bring the just processed

<sup>7</sup> <http://www.nucastrodata.org/infrastructure.html>

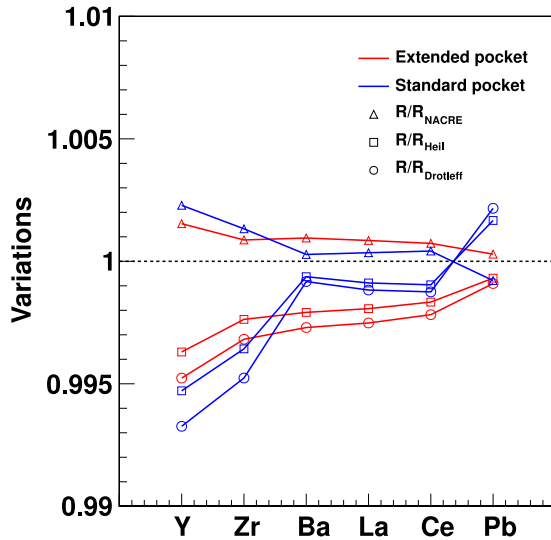


**Figure 19.** Variations of the abundances of the neutron-rich nuclei Y, Zr, Ba, La, Ce, and Pb for a star of 1.5 solar masses and  $Z = 0.01$ . Open triangles, squares, and circles refer to different ratios between the reaction rate of the present work and the rates of Angulo et al. (1999), Heil et al. (2008), and Drotleff et al. (1993), respectively. The horizontal dotted line indicates no variation in the mentioned elements abundances.

(A color version of this figure is available in the online journal.)

material from the interior to the surface of the star. To understand the changes in  $s$ -process yields due to our new rate, we selected a few elements that are most sensitive to reaction rate variations because of their position near neutron magic numbers. We chose, in particular, Y and Zr as the most representative nuclei of the ls-peak (ls for light), Ba, La, and Ce for the peak of heavier (hs) elements, and Pb, more specifically  $^{208}\text{Pb}$ , because it is placed near the  $s$ -process termination point.

The variations of the abundances of the selected elements in the He-rich region are shown in Figure 19 for several ratios between the present THM  $^{13}\text{C}(\alpha, n)^{16}\text{O}$  reaction rate (R) and the same rates represented in Figure 18, except the La Cognata et al. (2012) one, which is a preliminary result. We performed the calculation assuming two different  $^{13}\text{C}$  pockets: the three red lines are obtained using the standard  $^{13}\text{C}$  reservoir as suggested by Gallino et al. (1998), while the effects of a more extended pocket, about four times deeper in mass than the previous one, are represented by blue points (see Maiorca et al. (2012) for more details). Figure 19 shows that all neutron-rich elements experience very limited changes in their respective abundances for every choice of the rate, although the He-rich region is subject to different neutron densities during radiative interpulse phases.

From an inspection of Figure 19, we can conclude that systematic behavior for Y, Zr, Ba, La, and Ce exists; in particular, their supply increases (red or blue open triangles) when we consider the ratio  $R/R_{\text{NACRE}}$  while, in the other two cases (squares and circles), their abundances decrease because of an increased rate of the  $^{13}\text{C}(\alpha, n)^{16}\text{O}$  reaction with respect to the ones in Heil et al. (2008) and Drotleff et al. (1993). The only exception is Pb that is synthesized, in the case of a standard pocket, by larger amounts using the THM rate instead of the Heil et al. (2008) or the Drotleff et al. (1993) ones, and is less produced in comparison with the NACRE rate (Angulo et al. 1999). However, because of the very small variations, of the order of few parts per thousand, it is impossible to draw realistic and unambiguous conclusions on the  $s$ -process element

distribution because of the large errors affecting both stellar models and observations.

A more detailed study of the effects of the new, improved  $^{13}\text{C}(\alpha, n)^{16}\text{O}$  reaction rate will be performed in the near future, extending the astrophysical analysis to different stellar models of low-mass AGB stars and focusing our attention on isotopic ratios (e.g.,  $^{87}\text{Kr}/^{85}\text{Kr}$ ,  $^{86}\text{Rb}/^{82}\text{Rb}$ , etc.). A different neutron density and flux, already pointed out for the cases presented in this paper, might modify the relative abundances of isotopes placed in correspondence of branching points and could be crucial for an accurate determination of the solar element distribution.

The work was supported by the Italian MIUR under grant No. RBFR082838. G.G.K. acknowledges support from OTKA (PD104664) and the János Bolyai Research Scholarship of the Hungarian Academy of Sciences. A.M.M. acknowledges support from the US Department of Energy under Grant Nos. DE-FG02-93ER40773 and DE-SC0004958 (topical collaboration TORUS) and NSF under grant No. PHY-0852653. O.T. is grateful to Fondazione Cassa di Risparmio di Perugia for financial support and to professor M. Busso for his help in the nucleosynthesis calculations.

## REFERENCES

- Aliotta, M., Raiola, F., Gyürky, G., et al. 2001, *NuPhA*, **690**, 790  
 Angulo, C., Arnould, M., Rayet, M., et al. 1999, *NuPhA*, **656**, 3  
 Angulo, C., Engstler, S., Raimann, G., et al. 1993, *ZPhyA*, **345**, 231  
 Araki, T., Enomoto, S., Furuno, K., et al. 2005, *Natur*, **436**, 499  
 Assenbaum, H. J., Langanke, K., & Rolfs, C. 1987, *ZPhyA*, **327**, 461  
 Bair, J., & Haas, F. 1973, *PhRvC*, **7**, 1356  
 Barker, F. C. 2002, *NuPhA*, **707**, 277  
 Blatt, J. M., & Biedenharn, L. C. 1952, *RvMP*, **24**, 258  
 Bracci, L., Fiorentini, G., Melezhik, V. S., Mezzorani, G., & Quarati, P. 1990, *NuPhA*, **513**, 316  
 Brune, C. R., Licot, I., & Kavanagh, R. W. 1993, *PhRvC*, **48**, 3119  
 Busso, M., Gallino, R., & Wasserburg, G. J. 1999, *ARA&A*, **37**, 239  
 Costanzo, E., Lattuada, M., Romano, S., Vinciguerra, D., & Zadro, M. 1990, *NIMPA*, **295**, 373  
 Davids, C. 1968, *NuPhA*, **110**, 619  
 Descouvemont, P. 1987, *PhRvC*, **36**, 2206  
 Drotleff, H. W., Denker, A., Knee, H., et al. 1993, *ApJ*, **414**, 735  
 Dufour, M., & Descouvemont, P. 2005, *PhRvC*, **72**, 015801  
 Engstler, S., Raimann, G., Angulo, C., et al. 1992, *ZPhyA*, **342**, 471  
 Fiorentini, G., Kavanagh, R. W., & Rolfs, C. 1995, *ZPhy*, **350**, 289  
 Gallino, R., Arlandini, C., Busso, M., et al. 1998, *ApJ*, **497**, 388  
 Greife, U., Gorris, F., Junker, M., Rolfs, C., & Zahnw, D. 1995, *ZPhyA*, **351**, 107  
 Gulino, M., Spitaleri, C., Cherubini, S., et al. 2010, *JPhG*, **37**, 125105  
 Guo, B., Li, Z. H., Lugaro, M., et al. 2012, *ApJ*, **756**, 193  
 Hale, G. M. 1997, *NuPhA*, **621**, 177  
 Harissopoulos, S., Becker, H. W., Hammer, J. W., et al. 2005, *PhRvC*, **72**, 062801  
 Heil, M., Detwiler, R., Azuma, R. E., et al. 2008, *PhRvC*, **78**, 025803  
 Herwig, F. 2005, *ARA&A*, **43**, 435  
 Iliadis, C. 2007, *Nuclear Physics of Stars* (Weinheim: Wiley-VCH Verlag)  
 Jain, M., Roos, P. G., Pugh, H. G., & Holmgren, H. D. 1970, *NuPhA*, **153**, 49  
 Johnson, E. D., Rogachev, G. V., Mukhamedzhanov, A. M., et al. 2006, *PhRvL*, **97**, 192701  
 Käppeler, F., Gallino, R., Bisterzo, S., & Aoki, W. 2011, *RvMP*, **83**, 157  
 Keeley, N., Kemper, K. W., & Khoa, D. T. 2003, *NuPhA*, **726**, 159  
 Kellogg, S., Vogelaaar, R., & Kavanagh, R. 1989, *BAPS*, **34**, 1192  
 Kubono, S., Abe, K., Kato, S., et al. 2003, *PhRvL*, **90**, 062501  
 La Cognata, M., Goldberg, V. Z., Mukhamedzhanov, A. M., Spitaleri, C., & Tribble, R. E. 2009, *PhRvC*, **80**, 012801  
 La Cognata, M., Mukhamedzhanov, A. M., Spitaleri, C., et al. 2011, *ApJL*, **739**, L54  
 La Cognata, M., Romano, S., Spitaleri, C., et al. 2007, *PhRvC*, **76**, 065804  
 La Cognata, M., Spitaleri, C., Mukhamedzhanov, A., et al. 2010a, *ApJ*, **708**, 796  
 La Cognata, M., Spitaleri, C., Mukhamedzhanov, A., et al. 2010b, *NuPhA*, **834**, 658

- La Cognata, M., Spitaleri, C., & Mukhamedzhanov, A. M. 2010c, *ApJ*, **723**, 1512
- La Cognata, M., Spitaleri, C., Trippella, O., et al. 2012, *PhRvL*, **109**, 232701
- La Cognata, M., Spitaleri, C., Tumino, A., et al. 2005, *PhRvC*, **72**, 065802
- Lamia, L., Spitaleri, C., Burjan, V., et al. 2012, *JPhG*, **39**, 015106
- Lane, A. M., & Thomas, R. G. 1958, *RvMP*, **30**, 257
- Mahaux, C., & Weidenmüller, H. A. 1969, *Shell-Model Approach to Nuclear Reactions* (Amsterdam: North-Holland)
- Maiorca, E., Magrini, L., Busso, M., et al. 2012, *ApJ*, **747**, 53
- Meadows, J. W. 1967, *PhRv*, **157**, 1076
- Messiah, A. 1962a, *Racah Coefficients and '6j' Symbols*. Appendix C.II in *Quantum Mechanics*, Vol. 2 (Amsterdam: North-Holland), 567
- Messiah, A. 1962b, *Clebsch-Gordan (C.-G.) Coefficients and '3j' Symbols*. Appendix C.I in *Quantum Mechanics*, Vol. 2 (Amsterdam: North-Holland), 1054
- Meyer, B. 1994, *ARA&A*, **32**, 153
- Mukhamedzhanov, A. M. 2011, *PhRvC*, **84**, 044616
- Mukhamedzhanov, A. M., Blokhintsev, L. D., Irgaziev, B. F., et al. 2008, *JPhG*, **35**, 014016
- Mukhamedzhanov, A. M., Clark, H. L., Gagliardi, C. A., et al. 1997, *PhRvC*, **56**, 1302
- Mukhamedzhanov, A. M., La Cognata, M., & Kroha, V. 2011, *PhRvC*, **83**, 044604
- Mukhamedzhanov, A. M., Timofeyuk, N. K., & Tribble, R. E. 1995, *PhRvC*, **51**, 3472
- Mukhamedzhanov, A. M., & Tribble, R. E. 1999, *PhRvC*, **59**, 3418
- Ohlsen, G. G. 1965, *NIMPA*, **37**, 240
- Pellegriti, M. G., Hammache, F., Roussel, P., et al. 2008, *PhRvC*, **77**, 042801
- Pizzone, R. G., Spitaleri, C., Cherubini, S., et al. 2005, *PhRvC*, **71**, 058801
- Pizzone, R. G., Spitaleri, C., Mukhamedzhanov, A. M., et al. 2009, *PhRvC*, **80**, 025807
- Rolfs, C., & Rodney, W. S. 1988, *Cauldrons in the Cosmos* (Chicago, IL: Univ. Chicago Press)
- Romano, S., Lamia, L., Spitaleri, C., et al. 2006, *EPJA*, **27**, 221
- Sergi, M. L., Spitaleri, C., La Cognata, M., et al. 2010, *PhRvC*, **82**, 032801
- Shapiro, I. S. 1967, in *Proc. XXXVIII International School of Physics "Enrico Fermi"*, ed. T. E. O. Ericson (New York: Academic Press), 210
- Shoppa, T. D., Koonin, S. E., Langanke, K., & Seki, R. 1993, *PhRvC*, **48**, 837
- Spitaleri, C., Lamia, L., Tumino, A., et al. 2004, *PhRvC*, **69**, 055806
- Spitaleri, C., Mukhamedzhanov, A. M., Blokhintsev, L. D., et al. 2011, *PAN*, **74**, 1725
- Straniero, O., Dominguez, I., Cristallo, S., & Gallino, R. 2003, *PASA*, **20**, 389
- Straniero, O., Gallino, R., Busso, M., et al. 1995, *ApJL*, **440**, L85
- The, L.-S., El Eid, M. F., & Meyer, B. S. 2000, *ApJ*, **533**, 998
- Thielemann, F.-K., Arnould, M., & Truran, J. 1987, in *Advances in Nuclear Astrophysics*, ed. A. Vangioni-Flam (Gif-sur-Yvette: Editions Frontiere), 525
- Thomas, R. G. 1951, *PhRv*, **81**, 148
- Thompson, I. J. 1988, *CoPhR*, **7**, 167
- Thompson, I. J., & Nunes, F. M. 2009, *Nuclear Reactions for Astrophysics: Principles, Calculation and Applications of Low-Energy Reactions* (Cambridge: Cambridge Univ. Press)
- Tilley, D. R., Weller, H. R., & Cheves, C. M. 1993, *NuPhA*, **564**, 1
- Tumino, A., Spitaleri, C., Mukhamedzhanov, A., et al. 2007, *PhRvL*, **98**, 252502
- Tumino, A., Spitaleri, C., Mukhamedzhanov, A., et al. 2008, *PhRvC*, **78**, 064001
- Tumino, A., Spitaleri, C., Mukhamedzhanov, A. M., et al. 2011, *PhLB*, **700**, 111
- Zahnow, D., Rolfs, C., Schmidt, S., & Trautvetter, H. P. 1997, *ZPhyA*, **359**, 211